

MAXIMA: A BALLOON-BORNE COSMIC MICROWAVE BACKGROUND ANISOTROPY EXPERIMENT

B. RABII^{1,2,3}, C. D. WINANT^{1,2,3}, M. E. ABROE⁴, P. ADE⁵, A. BALBI⁶, J. J. BOCK^{7,8}, J. BORRILL^{2,9}, A. BOSCALERI¹⁰,
 P. DE BERNARDIS¹¹, J. S. COLLINS^{1,2}, P. G. FERREIRA¹², S. HANANY^{3,4}, V. V. HRISTOV⁷, A. H. JAFFE^{3,13},
 B. R. JOHNSON⁴, A. E. LANGE⁷, A. T. LEE^{1,2,3}, C. B. NETTERFIELD¹⁴, E. PASCALE¹⁰, P. L. RICHARDS^{1,3}, G. F. SMOOT^{1,15},
 R. STOMPOR^{2,9}, J. H. P. WU^{3,16}

Draft version February 2, 2008

ABSTRACT

We describe the Millimeter wave Anisotropy eXperiment IMaging Array (MAXIMA), a balloon-borne experiment designed to measure the temperature anisotropy of the Cosmic Microwave Background (CMB) on angular scales of $10'$ to 5° . MAXIMA mapped the CMB using 16 bolometric detectors in spectral bands centered at 150 GHz, 240 GHz, and 410 GHz, with $10'$ resolution at all frequencies. The combined receiver sensitivity to CMB anisotropy was $\sim 40 \mu\text{K} \sqrt{\text{sec}}$. Systematic parasitic contributions were minimized by using four uncorrelated spatial modulations, thorough crosslinking, multiple independent CMB observations, heavily baffled optics, and strong spectral discrimination. Pointing reconstruction was accurate to $1'$, and absolute calibration was better than 4%. Two MAXIMA flights with more than 8.5 hours of CMB observations have mapped a total of 300 deg^2 of the sky in regions of negligible known foreground emission. MAXIMA results have been released in previous publications. MAXIMA-I maps, power spectra and correlation matrices are publicly available at <http://cosmology.berkeley.edu/maxima>.

Subject headings: cosmic microwave background

1. INTRODUCTION

MAXIMA was a balloon-borne experiment designed to measure the anisotropy of the CMB over a wide range of angular scales ($\ell = 35$ to 1000). High resolution observations were made of 300 deg^2 of the sky over the course of two flights, in 1998 and 1999. Results have been released (Lee et al. (2001), Hanany et al. (2000)) and cosmological implications have been explored from both the MAXIMA data set alone (Stompor et al. (2001), Abroe et al. (2002), Balbi et al. (2000), Cayon, Argueso, & Martinez-Gonzalez (2003)) and combined with other data sets (Jaffe et al. (2001), Sievers et al. (2003), Rubino-Martin et al. (2003), Goldstein et al. (2003)). Abroe et al. (2003) presents correlations of MAXIMA data with those from the Wilkinson Microwave Anisotropy Probe (Spergel et al.

¹ Dept. of Physics, University of California, Berkeley, CA 94720, USA

² Space Sciences Laboratory, University of California, Berkeley, CA 94720, USA

³ Center for Particle Astrophysics, University of California, Berkeley, CA 94720, USA

⁴ School of Physics and Astronomy, University of Minnesota/Twin Cities, Minneapolis, MN 55455, USA

⁵ Cardiff University, Physics Department, Cardiff CF24 3YB, UK

⁶ Universitá di Roma Tor Vergata, 00133 Roma, Italy

⁷ California Institute of Technology, Pasadena, CA 91125, USA

⁸ Jet Propulsion Laboratory, Pasadena, CA 91109, USA

⁹ Computational Research Division, Lawrence Berkeley National Laboratory, Berkeley, CA 94720, USA

¹⁰ IFAC-CNR, 50127 Firenze, Italy

¹¹ Universitá di Roma La Sapienza, I-00185 Roma, Italy

¹² Astrophysics and Theoretical Physics, University of Oxford, Oxford OX1 3RH, UK

¹³ Imperial College, London SW7 2BW, UK

¹⁴ Physics Department, University of Toronto, Toronto, ON M5S 3H8, Canada

¹⁵ Physics Division, Lawrence Berkeley National Laboratory, Berkeley, CA 94720, USA

¹⁶ Dept. of Physics, National Taiwan University, Taipei 106, Taiwan

2003).

This paper, which is derived from two Ph.D. dissertations (Rabii (2002), Winant (2003)), is an overview of the experimental design and achieved performance of MAXIMA. Section 2 describes the two MAXIMA science flights. Section 3 describes the optics and optical characterization. Section 4 describes the detector system. Section 5 describes the cryogenic receiver and support electronics. Section 6 discusses the in-flight responsivity calibration. Section 7 presents the pointing system and attitude reconstruction.

1.1. Goals

The primary scientific objectives of MAXIMA were to distinguish between the inflationary paradigm and the topological defect models for the evolution of the Universe, to measure the geometry of the Universe by identifying the location of the first peak in the CMB power spectrum and to provide information about other cosmological parameters. The ℓ -space coverage and resolution of the experiment were well suited for measurement of the first three acoustic peaks of adiabatic inflationary models. Measurements in this region have been a powerful tool for testing the general predictions of inflation and for parameter estimation. In the past few years, a number of experiments have published significant measurements of this type (Spergel et al. (2003), Wang et al. (2002)).

MAXIMA data have also been used to test analysis methods and tools. Treatments have been developed for problems such as beam asymmetry (Wu et al. 2001b), foreground discrimination (Jaffe et al. 2002), scan synchronous noise (Stompor et al. 2002)), and detection of spatial non-Gaussianity (Wu et al. (2001a), Santos et al. (2003), Santos et al. (2002)).

MAXIMA has been used to test new technologies. In particular, MAXIMA was the first CMB experiment to

have used ~ 100 -mK spider-web bolometers, similar to those planned for the Planck Surveyor. The combination of these detectors and an adiabatic demagnetization cooling system has provided receiver sensitivity of $\sim 40 \mu\text{K} \sqrt{\text{sec}}$, the best reported by any CMB experiment.

The primary scientific result from MAXIMA is the angular power spectrum shown in Figure 1 (Lee et al. 2001).

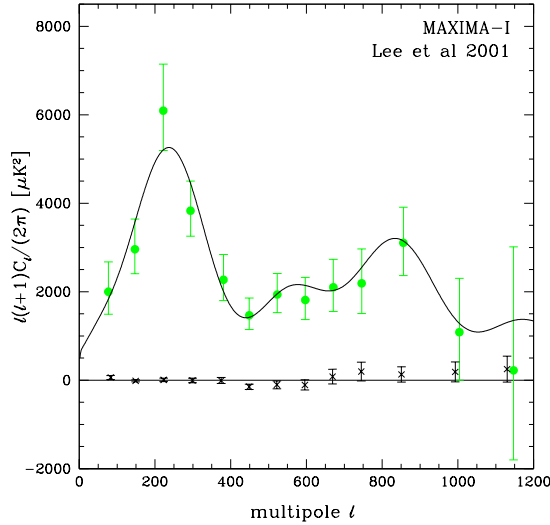


FIG. 1.— The power spectrum of the CMB using a hybrid analysis of $5'$ resolution (up to $l = 335$) and $3'$ resolution (over $l = 335$) maps. Error bars show the statistical uncertainties. The solid curve is the power spectrum of the best fit model from Balbi et al. (2000) with $\Omega_b = 0.1$, $\Omega_{cdm} = 0.6$, $\Omega_\Lambda = 0.3$, $n = 1.08$, and $h = 0.53$. The crosses are the power spectrum of the difference between the map from one detector and the combined map from the other two detectors used for the $3'$ analysis. (Lee et al. (2001))

1.2. Technical Overview

MAXIMA was a bolometric instrument which measured CMB temperature fluctuations in frequency bands centered at 150 GHz, 240 GHz, and 410 GHz. In order to avoid atmospheric emission, observations were made from an altitude of ~ 40 km during multiple balloon flights. The relatively short duration of the balloon-borne observations was offset by the use of a 16-element array of single color photometers with extremely sensitive detectors. The telescope was an off-axis Gregorian system with a 1.3-m diameter primary mirror providing a $10'$ beam size (FWHM) for all detectors. The combination of this angular resolution and ~ 100 square degrees of sky coverage made the experiment sensitive over a wide range of angular scales. The compact and well cross-linked scan pattern was optimized for extracting the angular power spectrum. The use of three spectral bands allowed discrimination between the CMB and foreground sources. MAXIMA benefited from precise pointing reconstruction ($1'$ rms) and accurate calibration (4%). The instrument was designed to survive repeated balloon flights and has been successfully recovered after five flights, including two MAXIMA science flights. A mechanical drawing of the MAXIMA telescope can be seen in Figure 2.

2. OBSERVATIONS

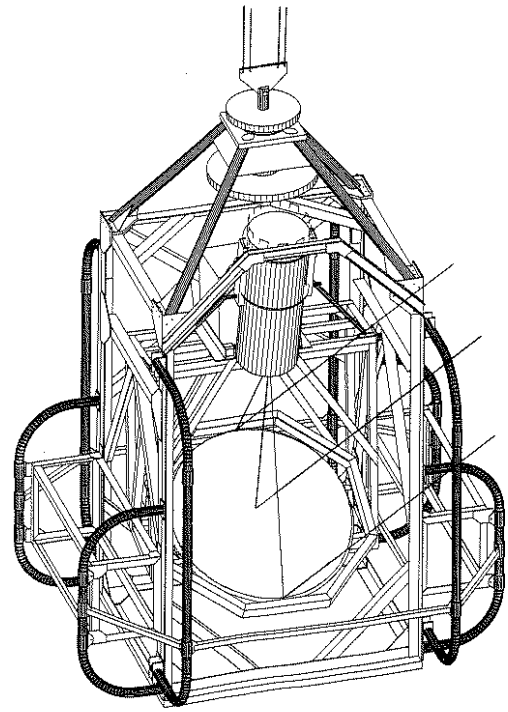


FIG. 2.— A mechanical drawing of the MAXIMA telescope from an elevated front/side perspective. Rays representing the telescope beam are shown reflecting from the primary mirror into the cryogenic receiver. Electronics housed in the rectangular boxes on the sides of the instrument include the pointing system, data multiplexers and digitizers, and telemetry and command interfaces. Near the top of the telescope are motors controlling azimuthal orientation. The inner assembly consisting of the primary mirror and the receiver is tilted relative to the outer frame to aim the telescope in elevation. The gondola frame is covered in lightweight aluminum-covered builders foam (not shown) and the primary mirror is surrounded by a scoop built of aluminum sheet (not shown), both of which shield the telescope and receiver from stray optical and radio frequency radiation.

The first science flight, MAXIMA-I, was launched on 1998 August 2 at 00:58 UT (1998 August 1, 19:58 local time) from the National Scientific Balloon Facility (NSBF) in Palestine, TX (latitude 31.8°N , longitude 95.7°W). The maximum float altitude of 37.5 km was reached at 4:35 UT. The telescope traveled 189 km west and less than 1 km south before reaching maximum altitude. At float, the telescope drifted 405 km west and less than 1 km north. Descent began 3.8 hours later at 8:22 UT. Summer flights from the NSBF in Palestine are limited to a range of approximately 600 km. The MAXIMA-I flight was relatively short due to fast high altitude winds.

Four observations were conducted during the flight. First, the CMB dipole was observed in order to calibrate the responsivity of the detectors. The dipole observation was started before reaching float altitude and lasted from 03:37 UT to 04:11 UT. Next, two overlapping, cross-linked scans of CMB anisotropy were conducted over a 122-deg^2 region in the vicinity of the Draconis constellation. These scans occurred from 04:21 UT to 05:59 UT and 06:02 UT to 07:24 UT. Finally, observations were made of Jupiter to characterize the telescope beams and to calibrate the 410-GHz detectors, which were insensitive to the CMB dipole. Jupiter was observed from 07:30



FIG. 3.— The MAXIMA telescope on the launch vehicle on 1999 June 16

UT until 08:04 UT.

The Sun was at least 20° below the horizon for all observations. The Moon was below 20° elevation during CMB observations, and below the horizon for over an hour of the second observation. While above the horizon, it was at least 70° from the scan region. The relative position of the Moon differed by 20° azimuth and 10° elevation between the two CMB scans. During the dipole observation, the Moon was at 30° elevation, 20° below the scan. The Moon was below the horizon during the Jupiter scan. The Moon was 68% full during the flight.

The instrument was launched a second time (MAXIMA-II) on 1999 June 17 at 00:07 UT (1999 June 16, 19:07 local time). Figure 3 is a photograph taken shortly before the launch. The telescope traveled 42 km east and 9 km south before reversing direction and reaching maximum altitude 97 km west and 1 km south of the launch position. The maximum float altitude of 38.0 km was reached at 04:34 UT. At float, the telescope drifted 490 km west and 42 km north. Descent began 7.8 hours later at 12:21 UT. The relatively slow high-altitude winds of early summer allowed us a considerably longer flight than MAXIMA-I.

As with MAXIMA-I, two CMB observations and two calibration scans were conducted. The first was an observation of Mars from 03:14 UT to 03:52 UT. Approximately one hour was spent on maintenance tasks. Two overlapping, cross-linked CMB scans were conducted from 05:04 UT to 07:29 UT and 07:31 UT to 09:40 UT. The observed region had an area of 225 deg^2 and overlapped the MAXIMA-I region by 50 deg^2 . A calibration scan of the CMB Dipole was conducted from 09:42 UT to 10:19 UT. Further data were recorded from 10:20 UT to 11:59 UT as a test of the daytime performance of the instrument.

The Sun rose to -20° elevation at 09:24 UT and to 0° elevation at 11:17 UT. Data collected after 10:20 UT have been used only as test data for future daytime balloon flights. The Moon was 17% full during the flight and was below the horizon during the dipole observation and both CMB observations. During the Mars observation, the Moon was 75° from the scan.

The scans for both flights are summarized in Table 1.

2.1. Sky Selection

TABLE 1
FLIGHT STATISTICS

Flight	Hrs at Max Alt	1st CMB Scan (hrs)	2nd CMB Scan (hrs)	CMB Dipole (hrs)	Planet Scan (hrs)	Daytime Test Data (hrs)
MAXIMA-I	3.78 ^a	1.63	1.37	0.57	0.57	0.00
MAXIMA-II	7.78	2.42	2.15	0.62	0.63	1.65

^a Some calibration data were collected before the telescope reached maximum altitude, resulting in a total scan time greater than the time at maximum altitude.

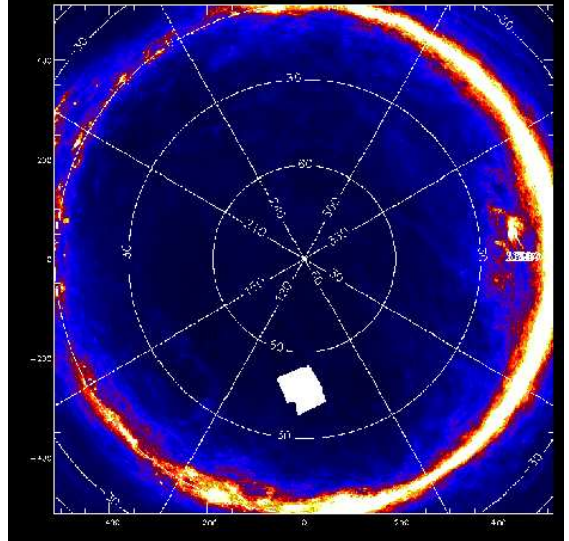


FIG. 4.— The MAXIMA-I CMB observation scan (white) is plotted over the Berkeley-Durham IRAS-Dirbe map of the northern galactic hemisphere dust emission extrapolated to 150 GHz (Finkbeiner, Davis, & Schlegel 1998). Areas of the sky with low dust contrast are shown as dark regions of the map. The MAXIMA-I CMB observation region is constrained to $b > 30^\circ$.

The main constraint on sky selection has been celestial foregrounds. The scan regions have a predicted dust temperature anisotropy of $\sim 10.0 \mu\text{K}$ at 150 GHz with rms fluctuations of $\sim 2.5 \mu\text{K}$ in units of equivalent CMB temperature fluctuation (Jaffe 1999). Tests of the spectral and angular profiles of the observed signals, as well as cross correlations with known dust maps, confirmed the absence of significant dust contamination in our CMB data (Jaffe et al. 2002). The MAXIMA-I scan region was chosen to contain no detectable point sources. For MAXIMA-II, this requirement was relaxed so that a few bright sources might be detectable in the anisotropy maps, particularly at 410 GHz. No point source contribution is expected in the CMB power spectrum. The MAXIMA-I scan region is shown overlaid with the IRAS-Dirbe dust map in Figure 4.

The scan regions for the two flights were chosen to have a modest ($\sim 50\text{-deg}^2$) overlap, both as a consistency check and to facilitate the combination of the data sets. The combined scan pattern is shown in Figure 5.

3. OPTICS

In order to achieve the desired sensitivity to CMB temperature fluctuations up to multipoles of $\ell \simeq 1000$, the

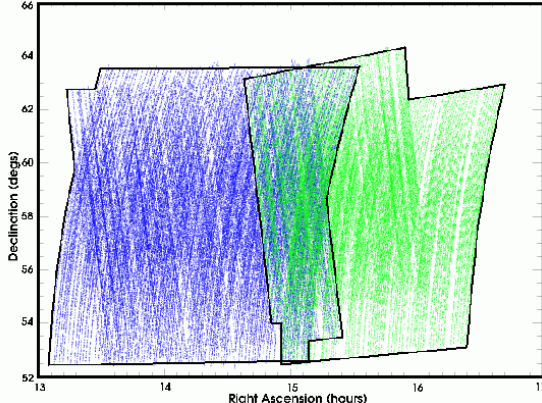


FIG. 5.— The full reconstructed pointing for a single detector in both MAXIMA flights. MAXIMA-I is the lighter region on the right, and MAXIMA-II is the darker region on the left. The scan region for each flight is boxed, and the $\sim 50\text{-deg}^2$ overlap region can be seen at Right Ascension ~ 15 hours.

telescope had an angular resolution of $10'$ FWHM. To make sure that local sources such as the Earth, the Moon and the balloon did not contaminate the measurement, we rejected side-lobe signals with a heavily baffled optical system. Optical background loading was on order of that from the CMB itself. Spectral bands were defined to distinguish CMB from atmosphere and celestial foregrounds.

3.1. Optical Design

3.1.1. The Telescope

The MAXIMA telescope was an off-axis Gregorian system, consisting of a ~ 1.3 m diameter underfilled primary mirror with cooled, baffled ellipsoidal secondary and tertiary mirrors. Figure 6 shows the optical system and Table 2 summarizes its optical properties.

The primary mirror was an off-axis section of a paraboloid, which was defined as the intersection of a cone and the paraboloid. The apex of the cone was at the focus of the parabola, had an opening angle of 52° , and was centered on an angle of 38° from the optical axis of the parabola. The focal length from the center of the mirror to the primary focus was 134 cm. The mirror was constructed by Dornier Satellitensysteme (Germany) from a light-weight graphite-epoxy honeycomb to facilitate modulation and weighs ~ 11 kg. The reflecting surface was made of 5000 Å of sputtered aluminum and a protective layer of 2000 Å of SiO₂. Bock measured the emissivity of samples of the surface near 150 GHz and found values between 0.27% and 0.6% Bock (1995a). Contour measurements gave an RMS surface accuracy of $8.3 \mu\text{m}$ with fixed focus position and $8.1 \mu\text{m}$ with a shift of focus of 0.61 mm. The mirror was fabricated from the pattern made for the 3-m Cologne mm-wave telescope to reduce fabrication costs.

The design of the reimaging system was driven by the fixed optical parameters of the primary mirror, a need for a cooled aperture stop (Lyot stop) and a requirement for a diffraction limited field of view of one square degree at frequencies lower than about 420 GHz. It was also preferable to cool the secondary optics to reduce the optical load on the detectors because emission from

TABLE 2
OPTICAL PARAMETERS OF THE MAXIMA TELESCOPE.

System Parameters	
Effective Pupil Diameter	835 mm
System Focal Length	1521 mm
Focal Ratio	1.8
Plate Scale	0.4 deg cm ⁻¹
Primary Mirror	
Dimensions	1328 mm \times 1267 mm
Conic Constant ^a	-1
Vertex Radius of Curvature	2400 mm
Focal Length	1340 mm
Secondary Mirror	
Radius	210 mm
Conic Constant	-0.126
Vertex Radius of Curvature	168 mm
Aspheric coefficients ^a	$A = 2.15 \times 10^{-5}$ $B = -9.07 \times 10^{-8}$ $C = 1.55 \times 10^{-10}$
Tertiary mirror	
Radius	180 mm
Conic Constant	-0.227
Vertex Radius of Curvature	112.5 mm
Aspheric coefficients	$A = 6.59 \times 10^{-5}$ $B = -5.03 \times 10^{-7}$ $C = 1.58 \times 10^{-9}$

^a Surface parameters are given in terms of

$$z = \frac{cr^2}{[1 + \sqrt{1 - (1+k)c^2r^2}]} + Ar^4 + Br^6 + Cr^8$$

where z is the sag of the surface, c is the curvature at the vertex, k is the conic constant, and r is the perpendicular distance from the symmetry axis.

the telescope was expected to be a dominant source of detector noise at 150 GHz and 240 GHz, given the expected $\sim 10 \text{ nV Hz}^{-0.5}$ amplifier noise; see Table 3 and Section 4.2. Cooling the optics required a compact system.

The secondary optics consisted of ellipsoidal secondary and tertiary mirrors that had aspheric corrections and respective diameters of 21 cm and 18 cm. They were diamond turned from solid aluminum which gave an optical quality surface at visible wavelengths. The back of each mirror was lightweighted to reduce the mass and heat capacity. The mirrors were manufactured and assembled inside a baffled optics box by Speedring Systems (U.S.A.). Speedring also used laser interferometry to verify the alignment and optical performance of the secondary optics. The optics box was housed within the MAXIMA cryostat and maintained at ~ 4 K by liquid helium. The interior baffles of the box were blackened with a ~ 0.5 cm thick layer of combined Stycast 2850 FT black epoxy, carbon lampblack, and 175- μm diameter glass beads, which has been demonstrated to be an effective far-infrared absorber (Bock 1994).

We used CODE V, a software package by Optical Research Associates, to design and assess the optical performance of the system. The telescope provided beams with full width at half maximum of $10'$ at all frequencies; at 150 GHz, 240 GHz, and 420 GHz the worst Strehl ratios (wave front errors) over the entire focal plane were 0.97 (0.03), 0.94 (0.04), and 0.83 (0.07), respectively. (Strehl

TABLE 3
PREDICTED OPTICAL LOAD DURING FLIGHT

Source	P_{150} [pW]	P_{240} [pW]	P_{410} [pW]
CMB	0.11	0.10	0.01
Primary Mirror ^a	0.18	0.64	0.39
Atmosphere ^b	< 0.01	0.03	0.05
Optics Box ^c	0.10	0.10	0.01
Total	0.39	0.87	0.46

^a Assumed primary mirror emissivities of 0.5% and 0.6% for the 150, 240, and 410-GHz bands, respectively.

^b Atmospheric load was modeled with ATM

^c (Pardo, Cernicharo, & Serabyn 2001).

^c Approximation (factor of ~2).

ratios (wave front errors) larger (smaller) than 0.82 (0.06) are considered beyond the diffraction limit.). The focal surface was curved for which we accounted with the placement of the feedhorns. Figure 7 shows a schematic view of the focal plane from the point of view of the detectors.

We chose a Gregorian system with three foci because it could be well baffled; see Figure 6. A large Winston cone baffle was placed outside the cryostat window; a ray arriving from a direction away from the primary mirror required five edge diffractions with angles as large as 65° to arrive at the focal plane. The Winston cone baffled was designed to admit throughput only from the primary mirror.

During observations the primary mirror was modulated around an axis connecting the center of the primary mirror and its focus point. Less than 0.4% of the throughput was modulated on the primary mirror for any of the beams, minimizing offsets due to temperature or emissivity gradients.

3.1.2. Lyot Stop

We located the liquid ^4He cooled Lyot (aperture) stop after the tertiary mirror and before the entrance to the photometers to apodize the illumination of the primary and to terminate the excess field of view at ~ 4 K. The Lyot stop was fabricated from a 0.63-cm thick sheet of Eccosorb MF-124, a microwave absorber manufactured by Emerson & Cuming Microwave Products (U.S.A.). This thickness provided adequate absorption of excess radiation (Halpern et al. 1986).

The Lyot stop had an elliptical opening with semi-major and semi-minor axis lengths of 2.04 and 1.75 cm. We achieved a well focused beam despite the thickness of the material by tapering the opening to a knife edge at an angle of 30 degrees. The face pointed towards the sky is covered with a layer of $25\mu\text{m}$ aluminum foil which reflected radiation that would otherwise have been transmitted through the thinnest section of the taper.

3.1.3. Feedhorns

We used a feedhorn coupled array to shield the bolometers from instrumental optical load and from RFI. The use of feedhorn coupled systems is discussed in Griffin et al. (2002).

The optical signal from the sky was fed to 16 individual photometers through back-to-back circular aperture

copper feedhorns. At 150 GHz, 10' FWHM beams were at the diffraction limit of the telescope. We used single moded straight walled feedhorns at 150 GHz. The theoretical beam patterns for a single-moded straight walled feedhorn are well understood (Olver et al. 1994). The higher frequency channels were multi-moded and had Winston Cone feedhorns. The properties of Winston Cone feedhorns are explained in Welford & Winston (1978). All feedhorns were designed to create 10' FWHM beams. The back-to-back feedhorn design was used collimate the radiation, which was useful for spectral filtering.

The opening diameter of the feedhorns was quantified in terms of $NF\lambda$, where λ is the wave length of observation, F is the focal ratio (f-number) at the focal surface opening, and N is a numerical factor. F is determined by the beam FWHM and the reimaging scheme. The larger N is, the better control one has in defining the beam. However, increasing N separates the beams centers on the sky, which increases edge effects on the combined scan region. We optimized the aperture efficiency as described in Griffin et al. (2002) by choosing $N \simeq 2$ ($NF\lambda = (6.10:4.47)$ mm for the (150:240) GHz channel feedhorns). Though this choice separated the telescope beams by more than their 10' FWHM, our observation strategy did not require the beams to overlap.

The feedhorns were fabricated by machining aluminum mandrels to define the interior surface. The mandrels were then electroplated with copper, and the aluminum was etched away in a bath of NaOH. The exterior surfaces of the feedhorns were then trimmed on a lathe, and the interior surfaces were polished. The feedhorns and bolometer array are shown in Figure 8.

3.1.4. Frequency bands, filters and detector backshorts

MAXIMA observed in frequency bands centered at 150, 240, and 410-GHz. The 150 and 240-GHz bands were primarily used to measure the CMB. The 410-GHz band monitored emission from atmosphere, galactic dust, and extragalactic infrared point sources. Data from the three observation bands were used to discriminate spectrally between various signal sources.

The frequency bands were primarily defined by metal-mesh filters located in the relatively collimated beam between the feedhorns and the bolometers. The 240 and 410-GHz channels had both high-pass and low-pass metal-mesh filters. The 150-GHz channels only had a low-pass metal-mesh filter; the section of circular wave guide between the back-to-back straight cones acted as a high-pass filter.

The filters were built from thin metallic meshes supported on Mylar film substrates by P. Ade of Cardiff University, Cardiff, Wales (then at QMWC, London, England). The transmission of the filter was determined by the pattern and geometry of the film, and the number and spacing of the stack of meshes. A thin copper substrate was evaporated onto a taut $\sim 1.5\mu\text{m}$ thick Mylar sheet suspended on a stainless steel ring. The metal was patterned via photolithography in either a capacitive (low-pass), inductive (high-pass), or resonant (band-pass) geometry. The steepness of the cutoff was improved by stacking multiple meshes separated by $\lambda_0/4$, where λ_0 is the cutoff frequency of the filter. These filters can be repeatedly cryogenically cycled without any stress frac-

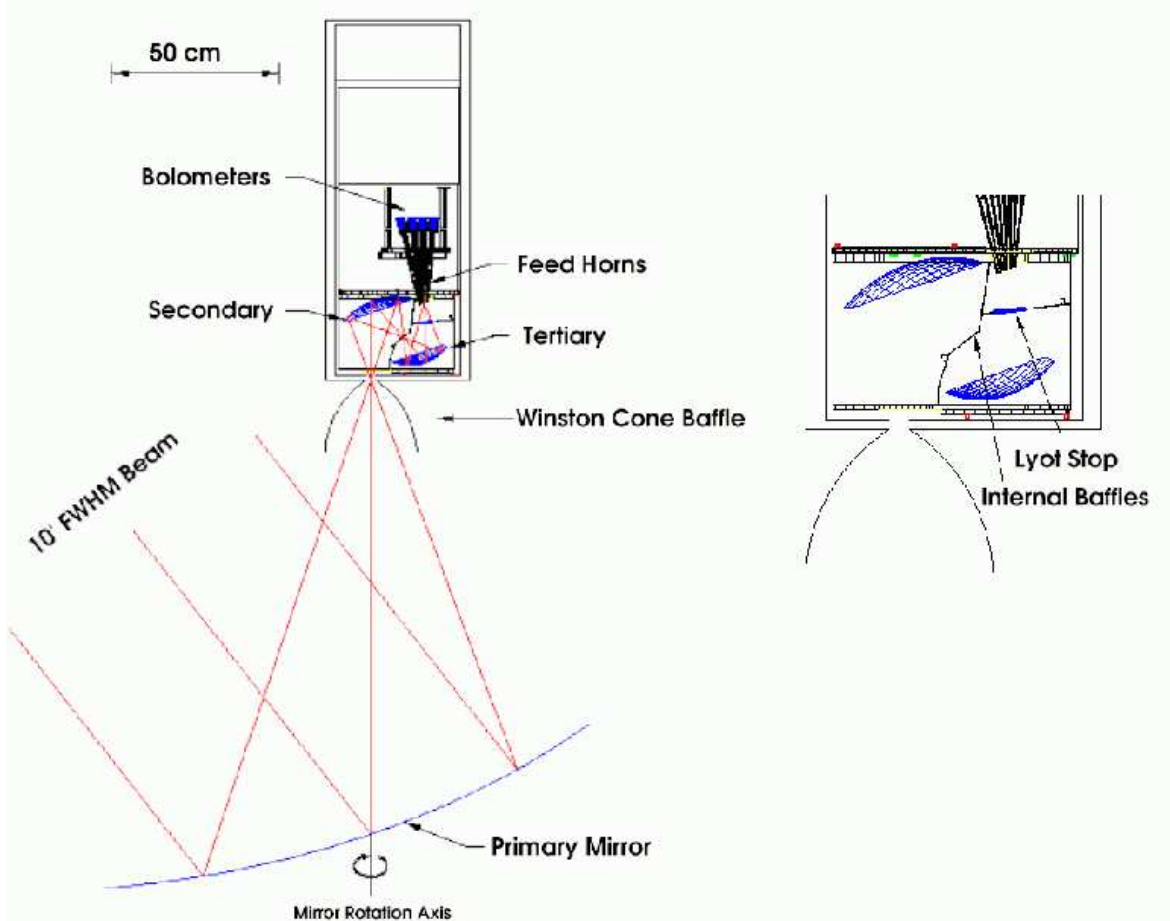


FIG. 6.— **Left:** The telescope was a fast ($f/1$) Gregorian system. The primary mirror, a 1.3-m diameter underilluminated paraboloid, was modulated about the indicated axis. A Winston cone baffle (shown outside the cryostat window) blocked radiation not reflected from the primary mirror. Cooled secondary and tertiary mirrors corrected aberrations from the primary. An array of feed horns channeled light to the bolometer cavities. Optical filters were located at the prime focus, the Lyot stop, and after the feed horns. **Right:** The focal plane was baffled from stray light in several ways. At least 5 edge diffractions with angles of up to 65 degrees were required for rays outside of the defined throughput to arrive to the focal plane. The internal baffles were blackened with mm absorptive material and the Winston cone baffle restricted the throughput to the area of the primary mirror.

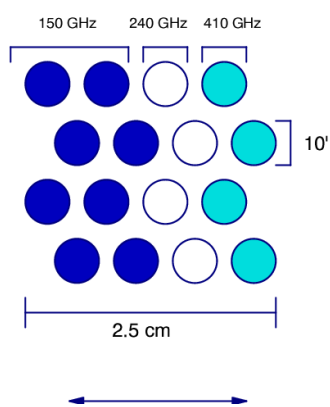


FIG. 7.— The layout of the MAXIMA focal plane as viewed from behind the bolometers. The arrows indicate the scan direction (azimuth modulation at constant elevation). All 16 channels project onto the sky with a $10'$ FWHM beam-size. The width of the focal plane was 2.5 cm.

tures or significant performance change. They have been demonstrated to have high transmission and sharp cut-

offs (Lee 1997).

The band defining filters leaked slightly at harmonics of the cutoff frequency. Three low-pass filters between the cryostat window and the entrance to the feedhorns blocked these leaks of the band defining-filters and provided overall rejection at higher frequencies. Two of these filters were low-pass metal-mesh filters with cut-offs at 480 GHz and 570 GHz. The last was an absorptive alkali-halide filter, and has a cutoff frequency of 1650 GHz.

The bolometers were suspended in resonant optical cavities with a depth of $\lambda_{obs}/4$, created by a flat brass backshort.

3.1.5. Neutral Density Filter

We placed a 1% transmitting neutral density filter (NDF) at the intermediate focus between the secondary and tertiary mirrors for optical tests with a 300-K load. The NDF was made by evaporating a thin continuous metal film onto a taut Mylar sheet stretched over a stainless steel ring, and was provided by P. Ade. The NDF was mounted on an aluminum slider which could be manually moved in and out of the beam using a vacuum-

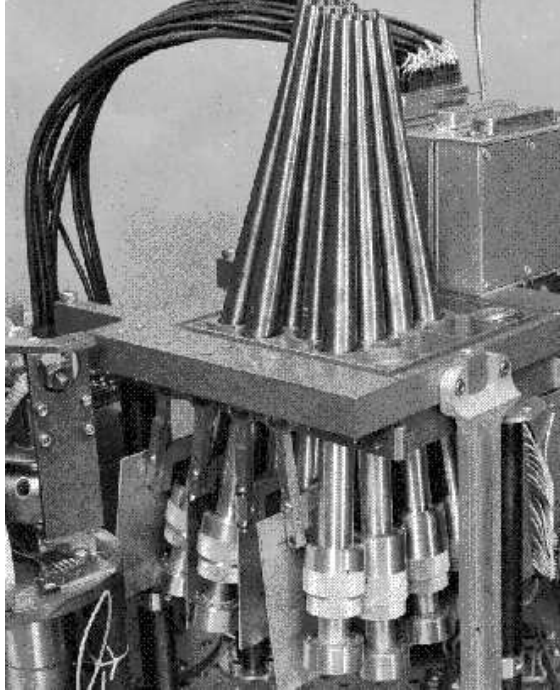


FIG. 8.— Photograph of feedhorns and bolometer array. The feedhorns (top of photograph) were assembled into a gold-plated aluminum plate. The band-defining metal mesh filters and bolometers for each photometer were stacked inside aluminum holders (bottom of photograph). The holders were assembled into a gold-plated aluminum plate that supported is by three thin-walled Vespel SP-22 legs. The horn and bolometer arrays were separated by a 0.5 mm gap at room temperature.

sealed linear actuator.

3.2. Pre-flight characterization

We measured the spectral response and optical efficiency of each channel in the laboratory before flight. We measured the beams of the entire telescope and the far side-lobe response of each channel just before flight to verify proper focusing and baffling of the telescope.

3.2.1. Spectral sensitivity

The transmission spectrum of each channel was measured before MAXIMA-I to verify the performance of the band defining filters. The spectra were used to discriminate between foreground and CMB signals and for calibration from point sources with spectra different from that of the CMB.

We measured the spectral response from 4.8 GHz to 1.2 THz, with a resolution of 4.8 GHz using a Michelson Fourier spectrometer (Richards 1967). One such spectrum from each of the three frequency bands is shown in Figure 9. The noise in the spectrum rose significantly below 90 GHz and above 1 THz due to the reduced efficiency of the beam splitter. We also saw increased noise at 540 GHz due to a strong water absorption line. We estimated a statistical error of 2% for the 150-GHz bands, 14% for the 240-GHz bands, and 7% for the 410-GHz bands.

The spectral response for all photometers of a given frequency band were morphologically similar. The FWHM band edges averaged over each set of detectors were

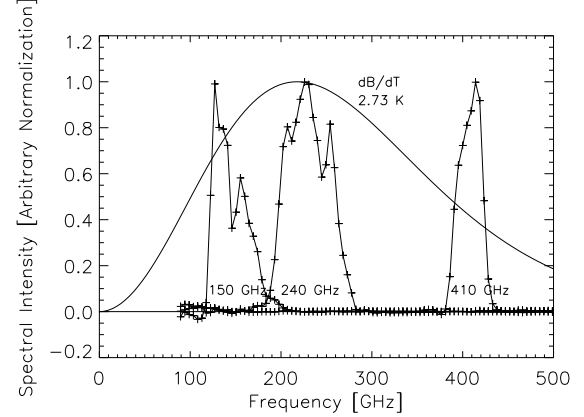


FIG. 9.— The measured, normalized spectral response for a detector of each color. The solid curve represents the derivative of the emission spectrum of a 2.73 K blackbody with respect to temperature, dB/dT . The spectra were measured before flight with a Michelson Fourier interferometer.

124 GHz to 164 GHz (150 GHz nominal), 199 GHz to 258 GHz (240 GHz nominal), and 393 GHz to 423 GHz (410 GHz nominal). This gave absolute (fractional) bandwidths of 40 GHz (27.8%) at 150 GHz, 59 GHz (25.8%) at 240 GHz, and 30 GHz (7.3%) at 410 GHz. The measured band centers varied by several GHz. In the case of the 150 GHz channels, the measured bands were asymmetric.

We checked for high frequency leaks in the photometers before each flight by measuring each bolometer's response to a Rayleigh-Jeans source (a chopped 77-300 K cold load) through a series of room-temperature high-pass filters. We placed a conservative estimate that $\sim 1\%$ or less of the chopped optical power detected by each bolometer leaked above the high-frequency cutoff of the nominal band for that photometer. This was a stringent test of susceptibility to foregrounds with steeply rising emission spectra over our observation bands ($B_\nu \propto \nu^x$, $x \geq 2$), such as galactic and extragalactic dust, the atmosphere, and albedo.

3.2.2. Optical Efficiency

The ratio of optical power detected to that which entered the telescope is less than unity. This frequency dependent quantity is the optical efficiency, $\epsilon(\nu)$. The total optical power detected, $P_{detected}$, can be expressed as

$$P_{detected} = A\Omega \int_{\nu_l}^{\nu_h} \epsilon(\nu) I(\nu) d\nu \simeq A\Omega <\epsilon(\nu)> \int_{\nu_l}^{\nu_h} I(\nu) d\nu, \quad (1)$$

where $A\Omega = 0.041 \text{ cm}^2 \text{ sr}$ is the throughput of the telescope, and $I(\nu)$ is the spectral intensity of the observed source. The average optical efficiency $<\epsilon(\nu)>$ is defined between FWHM frequencies ν_l and ν_h .

In the laboratory, we determined the average optical efficiency, $<\epsilon(\nu)>$, for each channel over its effective bandwidth. Using the neutral density filter to avoid saturation, we measured the load curve (*i.e.* bolometer resistance versus applied electrical power) of each bolometer with a 300-K optical load filling the throughput. We repeated the measurement with a 77-K load. For points

TABLE 4
OPTICAL EFFICIENCIES FOR THE MAXIMA RECEIVER

Channel	$\langle \nu \rangle$ [Hz]	$\langle \epsilon(\nu) \rangle$ [%]	Channel	$\langle \nu \rangle$ [Hz]	$\langle \epsilon(\nu) \rangle$ [%]
b14	150	18.4	b13	240	3.9
b15	150	8.4	b23	240	13.9
b24	150	20.2	b33	240	9.6
b25	150	22.8	b43	240	24.2
b34	150	14.2	b12	410	3.8
b35	150	-	b22	410	3.9
b44	150	16.8	b32	410	3.9
b45	150	15.0	b42	410	5.6

Note.—One channel was not functioning at the time of the measurement.

of equal resistance on the two load curves, the bolometer was electrically heated to an equal total (electrical plus optical) power; the difference in electrical power thus gave the difference in detected optical power from 300-K and 77-K.

We measured only the optical efficiency of the bolometers and the cold optics, as it was impractical to fill the primary mirror with a calibrated diffuse source. The primary mirror had an absorptivity of order 0.5% over all observation bands, and should degrade the overall optical efficiency minimally.

We made this series of measurements twice before MAXIMA-I. Between measurements, we polished the feed-horns and implemented $\lambda_0/4$ detector backshorts to improve the optical efficiencies. The efficiencies achieved are listed in Table 4.

3.2.3. Focusing

The telescope was focused by bringing the prime foci of the primary mirror and the secondary optics in the receiver together along a unique optical axis. This was initially done using mechanic alignment tools and visible laser tests. We then measured the two-dimensional beam profiles of each channel in the array by performing a raster scan with the telescope over a 7' FWHM source. The source was a halogen lamp mounted at the focus of a 1 m diameter $f/1$ paraboloidal mirror. The source was chopped at 5 Hz so that signal appeared above the 1/f knee in the bolometer signal bands. Measured profiles were compared to those predicted from simulations of the optical system with various types of defocus. We corrected the focus the telescope iteratively to minimize beam size and asymmetry. Beam contours for both observations are show in Figure 10.

3.2.4. Far side-lobe measurements

We measured the far side-lobe response of the telescope before flight to verify that sources such as the Earth, the Moon, the balloon, and the gondola would not contaminate our measurements of CMB temperature fluctuations.

We aimed a 150-GHz 20-mW Gunn oscillator at the assembled and baffled payload from a distance of ~ 20 m. The oscillator was chopped at 7 Hz. We performed the measurement outdoors to minimize secondary reflections off building walls. Nevertheless, it is likely that we detected some reflected signals, so the actual side-lobe sensitivity may be lower than the measurements indicate.

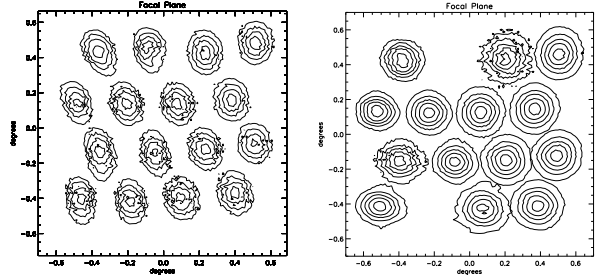


FIG. 10.—Beam contour plots for all channels in physical units. The beams are shown as projected onto the sky, which is the reverse point of view from that shown in Figure 7. **Left:** MAXIMA-I: the contours, moving from each beam center to each beam edge, represent the 90%, 70%, 50%, and 30% levels, respectively. **Right:** MAXIMA-II: the contours, from the center of each beam out, represent the 90%, 70%, 50%, 30%, and 10% levels respectively. Two of the 240 GHz channels were non-operational during the MAXIMA-II flight. Refinements in focusing techniques between the MAXIMA flights led to improved beam symmetry in MAXIMA-II.

For MAXIMA-I, the source was mounted on the top of a 35 m building for side-lobe measurements as a function of elevation angle. For MAXIMA-II, the source was mounted at the end of the arm of a “cherry picker” truck. The MAXIMA-II method more effectively minimized secondary reflections. We scanned across elevation and azimuth from the beam center yielding two orthogonal, one-dimensional side-lobe maps.

The response of the bolometers was linear for signal changes less than 20 dB. We attenuated the output of the source with both a dial-attenuator and 1-in (2.54-cm) thick sheets of plywood to keep the response linear over the 80 dB range of the measurement. We corrected for the attenuation of the source by measuring bolometer voltages before and after each change in attenuation at a fixed angle.

The measured far side-lobe response is shown in Figure 11. The measurement noise floor is roughly -75 dB. The elevation beam maps have a higher apparent noise floor, probably due to reflected signals. The measured attenuation at 15° below the beam is sufficient to prevent significant Earth-based side-lobe contamination. The apparent -60 dB back-lobe in MAXIMA-I is suspected to be an artifact of the measurement technique. Even if the back-lobe were real, no sources in the nighttime sky would be detectable with this attenuation.

3.3. In-flight characterization of beam patterns

The beam function (*i.e.*the Legendre polynomial expansion of the beam) is essential for probing CMB power at higher multipoles. We measured the beam patterns of each channel in the array during flight to determine the beam function, B_ℓ . Beam measurements were also necessary for point source responsivity calibration.

3.3.1. Measurement

The beam patterns were measured in flight by observing Jupiter for MAXIMA-I and Mars for MAXIMA-II. These planets were both small in angular size compared to the beam FWHM, and could thus be treated as point sources. They were detected with a signal-to-noise ratio of ~ 100 for Mars and ~ 1000 for Jupiter.

During planet observations, the telescope tracked the planet in azimuth while remaining at fixed elevation. As

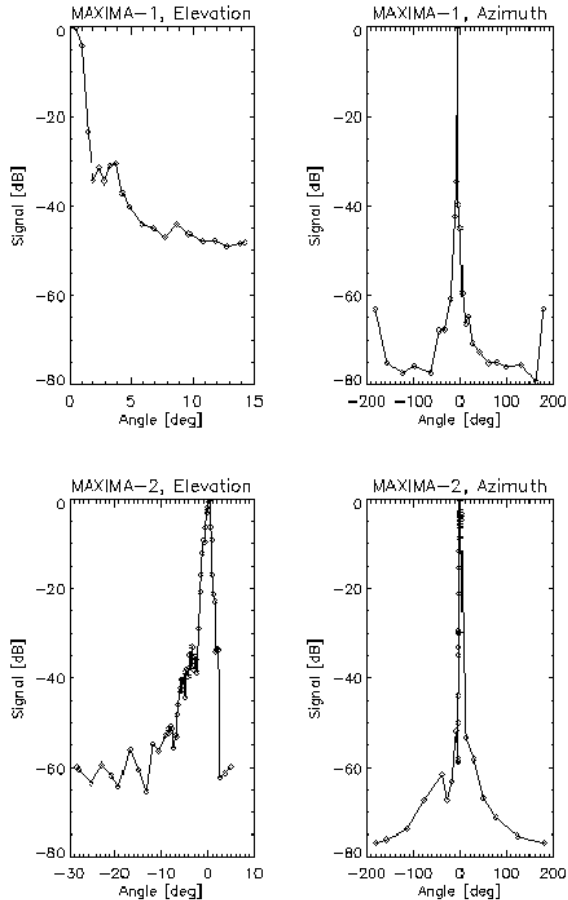


FIG. 11.— Data from pre-flight side-lobe tests. The source was roughly 30 m from the telescope. **Left Top:** Test data in the elevation direction for MAXIMA-I. The angle is that of the telescope above the test source. **Right Top:** Test data in the azimuth direction for MAXIMA-I. The telescope beam is at fixed elevation ($\sim 30^\circ$). The source is moved around the telescope at the same elevation. **Left Bottom:** As above, for MAXIMA-II. Most of these data were collected with the source at higher elevation than the telescope beam (negative angles on the x-axis). **Right Bottom:** As above, for MAXIMA-II.

the planet drifted through the elevation of the observation, the modulation of the primary mirror scanned the beams across the planet many times. As the planet drifted in elevation the spatial response of each beam was measured in two dimensions. The angular offset between the center of the beam and the boresight CCD camera was also measured in this scan. The detector data were averaged in fixed azimuth and elevation bins over a prescribed area and resolution through three-point linear interpolation. This beam map was decomposed into the beam function B_ℓ . We measured the beam FWHM from the 50% contour of the beam map.

We measured the beams for all of the functioning channels during both MAXIMA observations. Two-dimensional beam contours are shown in Figure 10. The FWHM of the major and minor axes of each beam is listed in Table 5.

3.3.2. Symmetry

During flight, the telescope revisited regions of the sky at different times so that the angle of the scan varies due to sky rotation. For fully symmetric beams, the same re-

TABLE 5
MAXIMA BEAMS FWHM

Channel	$< \nu >$ [GHz]	M1: θ_{maj} [arcmin]	M1: θ_{min} [arcmin]	M2: θ_{maj} [arcmin]	M2: θ_{min} [arcmin]
b14	150	11.3	9.0	10.0	9.3
b15	150	10.8	9.0	10.1	9.1
b24	150	10.8	8.4	9.5	9.2
b25	150	10.8	8.4	9.7	9.3
b34	150	10.8	8.4	9.5	9.5
b35	150	10.0	8.4	9.8	9.4
b44	150	10.5	9.2	10.1	9.3
b45	150	10.8	9.0	10.0	9.4
b13	240	10.2	8.4	- ^a	- ^a
b23	240	11.0	8.4	8.7	8.4
b33	240	11.3	7.7	8.7	8.2
b43	240	11.5	8.4	- ^a	- ^a
b12	410	12.0	8.3	8.8	8.1
b22	410	10.2	9.0	8.3	7.5
b32	410	13.6	7.9	8.5	8.1
b42	410	11.0	7.7	9.5	7.4

Note.— θ_{maj} and θ_{min} represent the major and minor axes. Values were determined from the 50% contour for each beam.

^a Non-operational channel

gion of the sky was observed upon revisit, regardless of angular orientation. Real beams have some degree of rotational asymmetry. Strict correction for this asymmetry would require that the beam function be expanded in a series of spherical harmonics (e.g., Abramovitz & Stegun (1972)).

Comparing the two panels in Figure 10, the beams in MAXIMA-II were noticeably more symmetric than those in MAXIMA-I. Our approach to this problem was to compute an effective, axially symmetric beam function, B_ℓ , and to estimate precisely an error incurred to such a procedure. Wu et al. (2001b) demonstrate that this approach is accurate for both MAXIMA flights.

3.3.3. Beam Characterization Uncertainty

We determined that the beam size uncertainty causes less than 4% and 11% uncertainty in the C_ℓ estimates for $\ell = 410$ and 785, respectively, and that beam asymmetry does not contribute significantly to power spectrum errors at any angular range. Complete beam errors contributions are reported in Lee et al. (2001) and Hanany et al. (2000).

Beam map uncertainties resulted from errors in the pointing reconstruction, detector noise, the uncertainties in the bolometer electronic filters and time response, and the limited area and resolution of the beam map. We list the contributions to the total error from these sources to the measured beam FWHM for one 150 GHz channel in Table 6. The total error is the quadrature sum of the individual contribution.

4. DETECTORS

The MAXIMA detector system was a 16-element bolometer array. A bolometer is a thermal detector whose electrical resistance varies as a function of temperature. This resistance is read out electrically. Thorough reviews of bolometers can be found in Richards (1994) and Galeazzi & McCammon (2003).

TABLE 6
SOURCES OF BEAM ERROR FOR ONE 150 GHz CHANNEL

Source of Error	σ_{fwhm} [arcmin]
White Noise in the Detector Time Stream	0.09
Bolometer Electronic Filters	0.13
Bolometer Time Constant	0.06
Phase Preserving Low-pass Filter	0.14
Pointing Reconstruction (differential err.)	0.05
Resolution of Beam Map	0.17
Area of Beam Map	0.15
Total	0.32

The audio frequency bandwidth of the bolometer signal must be wide enough to avoid constraining the ℓ -space coverage in the measurement of the power spectrum. The signal bandwidth is determined by the 1/f knee and the high frequency roll-off in the response of the instrument. Though some of the cosmological signal appeared at frequencies as low as the telescope scan frequency of ~ 20 mHz, it was primarily found above the 0.45 Hz frequency of the primary mirror modulation. Cosmological signals appeared as high as the the roll-off frequency of beam window function, as determined by the telescope scan speed. We set the high frequency roll-off of the electronic filters at 20 Hz, above the beam roll-off.

Low-frequency 1/f noise may cause striping in the maps, but it was effectively suppressed by cross-linked observations; sensitivity to large scale CMB fluctuations was mostly limited by observation area (sampling variance) but was also affected by residual 1/f noise.

The bolometer response time constrains the high-frequency cut-off of the signal band and limits the choice of scan speeds for the telescope. A slow detector response compared to the telescope scan speed has the effect of smearing the beams on the sky, distorting the window function. Hanany, Jaffe, & Scannapieco (1998) shows that to prevent significant distortion, bolometer response time must be at least 2.5 times faster than the time to scan a single beam size. This corresponded to a detector response time of 10 ms or less for our scans and beams.

4.1. MAXIMA bolometers

We used composite bolometers obtained from J. Bock at JPL (Figure 12). The bolometers were made with metallized mesh absorbers and neutron transmutation doped germanium (NTD-Ge) thermistors, the latter of which are obtained from J. Beeman and E. Haller at LBNL, Berkeley.

The temperature dependence of the electrical resistance of doped semiconductor thermistors has the form, $R(T) = R_0 \exp(\Delta/T)^{\frac{1}{2}}$, where $\Delta \sim 10$ K and is determined by the type and level of doping in the material.

The characteristic temperatures for the various types of NTD-Ge allow for operation between temperatures of 20 mK to 4.2 K. MAXIMA bolometers were made from NTD-19, which is optimized for operation at ~ 100 mK. More information on neutron transmutation doping can be found in Haller (1985).

Electrical contacts on the NTD-Ge chips were made through ion implantation, followed by a thermal anneal-

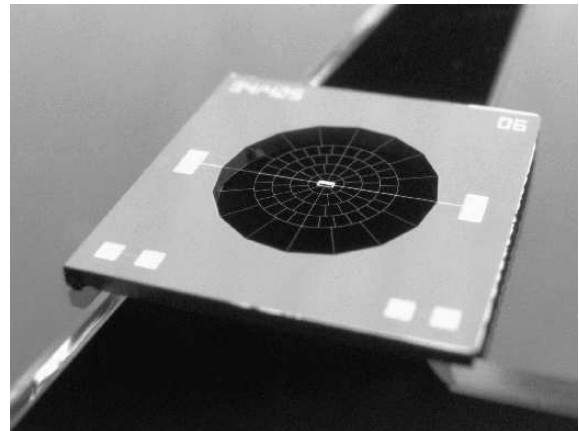


FIG. 12.— The bolometer pictured is of the same design as those used in MAXIMA. The spider-web absorber has a 2.5 mm diameter with a 5% filling factor. The radial components within the spider-web pattern are 160 μm long and 4 μm wide. The NTD-19 thermistor, a cube with 250 μm sides, is bump bonded to the center of the web. The chip is powered through two lithographed gold leads. Mechanical support comes from the electrical leads and sixteen silicon-nitride legs, 1 mm long and 5 μm wide. Photograph courtesy of J. Bock.

ing process. The wafers were metalized with a ~ 20 nm-thick layer of Cr or Ti, followed by a ~ 150 nm layer of Au for easy attachment of wires. The wafers were then diced, etched, and passivated. Gold leads were indium bump-bonded onto the metalized edges of the thermistor.

The bolometer absorbing structure was fabricated via optical lithography starting with a silicon on insulator (SOI) wafer coated with a 1 μm layer of silicon nitride (silicon-nitride). The top of the silicon-nitride was coated with a layer of gold whose thickness was selected to obtain an average sheet resistance of $377\Omega/\square$. A web with this sheet resistance absorbs 50% of the incoming radiation in one pass (Bock et al. 1995b). The absorber was then patterned in a ‘spider-web’ geometry with photoresist. A dry-etch was used to remove the gold and around the pattern. The SOI was dry etched from the back side of the wafer with deep trench Si etcher.

The spacing of the absorber legs was small enough to trap millimeter-wave radiation, but was large enough to let high energy cosmic rays pass through. The absorber had a 5% filling factor, which reduced its cosmic ray cross-section by $\sim 90\%$. The optical efficiency was further increased by placing the bolometers in an integrating cavity with a characteristic depth of $\lambda/4$.

4.2. Noise Characterization

The major contributors to bolometer noise are photon noise, Johnson noise, thermal fluctuation noise, and noise from the first stage of amplification (amplifier noise). A thorough discussion and derivation of each noise term is found in Richards (1994). Bolometer noise is generally discussed in the context of noise equivalent power, NEP, (or noise equivalent temperature, NET) which is defined as the incident signal power (or temperature) required to generate a signal equal to the noise in a one Hz bandwidth. The individual noise sources are uncorrelated. The total noise is given by the sum of each term in quadrature.

We choose the thermal conductance G required to re-

TABLE 7
AVERAGE BOLOMETER THERMAL PROPERTIES

Observation Frequency ν	Thermal Conductance <math>< G ></math>	Temperature Rise <math>< \frac{\Delta T}{T_0} ></math>
[Hz]	[pW K $^{-1}$]	
150	71	0.51
240	290	0.29
410	320	0.21

duce the contribution of thermal fluctuation noise compared to photon noise (Table 7). We operated the bolometers at a bath temperature of $T_0 \approx 100$ mK, which is cold enough that thermal fluctuation noise is less than the photon noise. We used low noise JFET pre-amplifiers. We constrained these various parameters with the help of computer-generated models, such as the one shown in Figure 13.

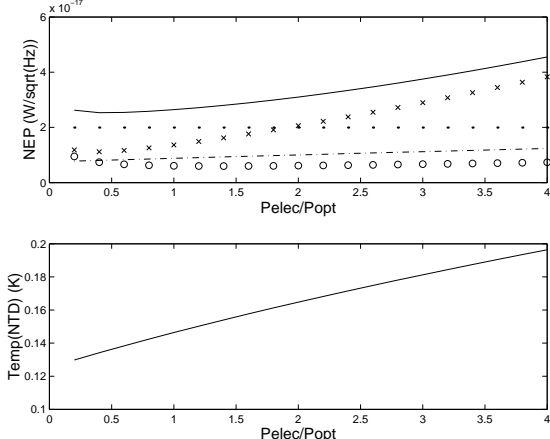


FIG. 13.— Bolometer noise simulation. The top panel is a plot of the contributions to the bolometer NEP as a function of the ratio of the electrical power, P_{elec} to the optical power, P_{opt} . The contributions are thermal fluctuation noise (dot-dash), Johnson noise (circles), and amplifier noise (crosses), photon noise (dotted). The solid line is the quadrature sum of the terms. The bottom panel is a plot of the thermistor temperature as a function of the same ratio of powers. We assume an operating temperature, T_{base} of ~ 100 mK, an optical load, P_{opt} , of 2 pW, an average thermal conductance, G of 70 pW K $^{-1}$, and JFET voltage noise, e_n of $6nV\ Hz^{-0.5}$.

We computed bolometer noise power spectra from a subset of the data during the CMB observations. We found the frequency power spectrum out to the Nyquist frequency of 104 Hz. A typical noise power spectrum is shown in Figure 14. The spectrum can be divided into three frequency ranges. For frequencies below ~ 100 mHz, the spectrum decreases as $1/f$. At intermediate frequencies, the noise spectrum is white. At frequencies above ~ 20 Hz, the spectrum decreases because of the electronic low-pass filter and bolometer time constant. Noise measurements for all functioning channels are presented for MAXIMA-I in Table 8 and for MAXIMA-II in Table 9. The voltage noise was determined from the average noise measured around a narrow audio frequency band (7.0 ± 0.2 Hz) near the center of the bolometer signal band. We assigned an uncertainty of $\sim 2nV\ Hz^{-0.5}$ to conservatively account for the non-uniformity of the white noise level over the signal band. This uncertainty did not take into account isolated peaks

TABLE 8
MAXIMA-I BOLOMETER CHARACTERIZATION

Channel	ν_{obs} [GHz]	V_n [$nV\ Hz^{-0.5}$]	NEP [$\times 10^{-17} W\ Hz^{-0.5}$]	NET_{cmb} [$\mu K\sqrt{\text{sec}}$]	τ [msec]
b14	150	16	2.8	130	12.5
b15	150	10	2.0	80	12.5
b24	150	18	4.0	170	12.5
b25	150	12	2.4	80	10.0
b34	150	12	1.8	75	7.0
b35	150	22	4.6	200	9.5
b44	150	38	6.8	230	10.5
b45	150	12	2.2	80	9.0
150_{comb}	150	5	0.9	35	-
b13	240	14	3.4	380	10.5
b23	240	14	6.0	185	7.0
b33	240	10	5.4	140	9.5
b43	240	24	9.8	345	9.0
240_{comb}	240	7	2.4	100	-
b12	410	18	6.6	-	12.0
b22	410	20	11.0	-	8.5
b32	410	24	7.6	-	6.0
b42	410	34	19.0	-	5.0
410_{comb}	410	11	4.4	-	-

Note.—Data from the channels in **bold** were used for the final data analysis.

in the noise spectra of microphonically sensitive detectors (see discussion below). These measurements served as a diagnostic of in-flight instrumental performance. A more sophisticated noise estimation, as described in Stompor et al. (2002), was used for finding CMB maps and angular power spectra. Tables 8 and 9 include the overall NEP and NET for the channels grouped by observation frequency.

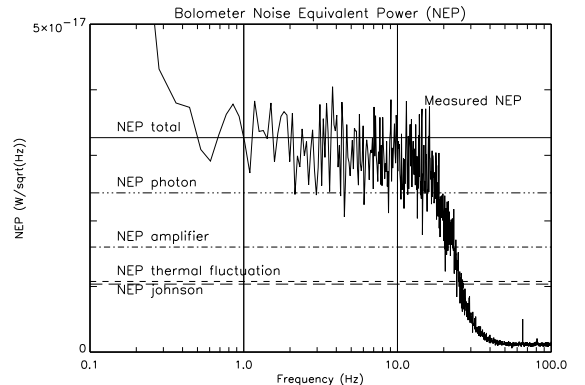


FIG. 14.— The measured noise equivalent power (NEP) spectrum for a 150 GHz MAXIMA bolometer plotted along with theoretical NEP contributions from photon (dotted), Johnson (long dash), thermal fluctuation (short dash), and amplifier (dot-dash) noise. The total NEP (solid line) is the quadrature sum of the terms. Low frequency noise below 0.4 Hz arises from temperature drifts in the cryogenic system. Electronic filters in the readout circuit cause the signal to roll off above 20 Hz

As the overall NEP for each channel was largely determined by a subset of the best performing bolometers, only these few were used for the published MAXIMA data analysis. Maps of CMB temperature anisotropy were made using three 150 GHz channels and one 240 GHz channel for MAXIMA-I and from four 150 GHz channels for MAXIMA-II. Data from these channels and from one

TABLE 9
MAXIMA-II BOLOMETER CHARACTERIZATION

Channel	ν_{obs} [GHz]	V_n [nV $Hz^{-0.5}$]	NEP [$\times 10^{-17} W Hz^{-0.5}$]	NET_{cmb} [$\mu K\sqrt{sec}$]	τ [msec]
b14	150	28	7.6	345	12.5
b15	150	10	2.4	65	11.5
b24	150	10	3.0	100	10.5
b25	150	10	2.8	80	12.0
b34	150	10	2.6	100	6.5
b35	150	8	2.4	90	8.0
b44	150	28	8.8	350	8.5
b45	150	10	2.8	85	8.5
150_{comb}	150	4	1.0	35	-
b13	240	-	-	-	-
b23	240	10	8.0	165	5.0
b33	240	12	6.0	170	8.5
b43	240	-	-	-	-
240_{comb}	240	8.8	4.8	120	-
b12	410	20	18	-	14.0
b22	410	12	16	-	6.5
b32	410	12	14	-	2.5
b42	410	20	24	-	3.0
410_{comb}	410	7	8.1	-	-

Note.-Data from the channels in **bold** were used for the Abroe et al. (2002) and Stompor et al. (2003) data analysis.

410 GHz channel were used for systematic tests, notably spectral discrimination of foreground signals.

For most MAXIMA-I channels, noise during CMB observations was stationary at the 10–20% level. A subset of the channels had high microphonic sensitivity and for these the NET value, which was calculated using a section of the data without microphonic noise, does not represent the effort involved in, or the expected benefit of analyzing the entire data set. These channels were not included in the final analysis. Most timestreams exhibited some degree of noise correlated with the spatial modulation of the primary mirror. This mirror synchronous signal proved to be stationary over long enough time scales, and we developed a formal template subtraction in subsequent analysis (Stompor et al. 2002). Low frequency noise rose as 1/f, with knees between 0.2 Hz and 0.6 Hz. Detector noise was Gaussian except near the chopper frequency. Frequencies below 0.1 Hz were poorly sampled and have been marginalized over in data analysis.

For MAXIMA-II, low frequencies noise rose more steeply than 1/f in all channels, with knees ranging from 1 Hz to 3 Hz. The source of the noise is unknown, and the time scale over which it was stationary varied between channels. In addition, mirror synchronous noise appeared in the higher observation frequency channels, especially during the beginning of the second CMB observation. The reported NEPs and NETs are not a complete reflection of the overall noise performance. Analysis of MAXIMA-II data (*e.g.* Abroe et al. (2003)) required marginalization over frequencies below 0.2 Hz.

4.3. Response Time Characterization

Measurements of the bolometer response times and noise were made during both the MAXIMA-I and MAXIMA-II flights. We determined the response times by deconvolving a single pole low-pass filter, whose characteristic frequency is a free parameter, from bolometer time

streams while scanning the primary telescope back and forth in azimuth across a planet. The bolometer time constant parameter was adjusted until the left and right going scans spatially coincided. This measurement had a statistical error of 0.50 msec. The measurements are presented in Tables 8 and 9 for MAXIMA-I and MAXIMA-II respectively. We replaced detectors in many channels between the two flights, which explains the difference in response time for many channels. In all cases, the measured response time was small enough to prevent significant beam smearing from the telescope modulation.

5. RECEIVER AND ELECTRONICS

The MAXIMA cryostat (Figure 15) housed the secondary optics, the bolometer array and preamplifiers, an optical calibration source, and the cryogenic system. There were also a number of diagnostic devices including ‘dark’ detector channels not exposed to the CMB and a variety of internal temperature monitors.

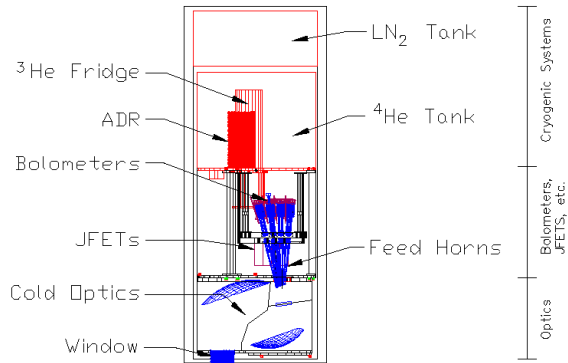


FIG. 15.—A mechanical drawing cutaway of the MAXIMA cryogenic receiver. The bottom section of the receiver contained baffled, liquid 4He -cooled optics and the internal relative calibration source. The middle held the bolometers and bolometer feedhorns, cryogenic JFET preamplifiers, and thermal switches. The top section of the receiver contained the cryogenic systems, with the low temperature refrigerators surrounded by the liquid 4He tank.

The cryostat was manufactured by Infrared Laboratories (model HDL14). It had an outer diameter of 40.5 cm and a length of 112.5 cm. Liquid N_2 and 4He were held in stainless steel-walled tanks, which were structurally supported by G-10 stand-offs. The coldplate for each tank was made of 1.9 cm thick gold-plated OFHC copper, which provides excellent thermal contact. The joint between the copper coldplate and the stainless steel wall of the 4He tank degraded after repeated thermal cycling over six years. We believe the weakness of the joint was due to differential thermal contraction over the large size of the tank. A replacement tank and coldplate were both constructed from aluminum to minimize differential thermal contraction.

5.1. Cryogenics

The detector array was cooled to ~ 100 mK during flight via a four-stage refrigeration process. The array was housed inside an evacuated cryostat, and was cooled by an adiabatic demagnetization refrigerator (ADR), which dumped its heat to a 3He sorption refrigerator backed by a pumped liquid 4He bath, and a pumped liquid N_2 bath. These cooling systems are summarized in Table 10.

TABLE 10
MAXIMA CRYOGENIC SYSTEMS

Cooler	Liquid N ₂	⁴ He	³ He	ADR
Temperature (K)	50	2-3	0.35	0.1
Hold Time (Hours)	24	>30	>36	12
Thermal Cycle	Open	Open	Closed	Closed

Note.-Numbers are quoted for flight conditions.

A 13-liter Liquid N₂ tank cooled an outer layer of radiation shielding to 77 K. This temperature dropped to ~50 K when the Liquid N₂ tank was exposed to vacuum, as in flight. The Liquid N₂ temperature radiation shields were covered with thin, low emissivity aluminum foil.

Inside the Liquid N₂-cooled space was a 21-liter liquid ⁴He tank and an additional layer of shielding at liquid ⁴He temperature. The outer shell of the cold optics box served as part of this radiation shielding. The outside of these shields was low emissivity aluminum, while the inner surfaces were coated with a blackening mixture. The blackened interior absorbed high temperature radiation that leaked past the shields.

Within the liquid ⁴He temperature space were the optics, the detectors, the JFET preamplifiers, the sub-Kelvin coolers, and a variety of thermometers. The optics and most electrical components were thermally linked to the coldplate.

Various locations in the liquid ⁴He space ranged in temperature from 4 K to 6 K, depending on thermal load and proximity to the helium tank. When the liquid ⁴He was exposed to vacuum, for testing or in flight, these temperatures drop to 2 K to 3 K. This caused a significant drop in the background loading of the bolometers.

Inset into the liquid ⁴He tank were the adiabatic demagnetization refrigerator (ADR) and the liquid ³He refrigerator. All wiring entering the receiver passed through the liquid ⁴He and Liquid N₂ tanks and was made of low thermal conductivity stainless steel leads.

5.1.1. ³He Refrigerator

We designed and constructed a large capacity ³He sorption refrigerator for the MAXIMA cryostat. The closed-cycle refrigerator consisted of 42 STP liters of ³He of 99.995% purity, an activated charcoal sorption pump, a copper condenser, and a copper evaporator which was hermetically coupled to the condenser with a thin-walled stainless steel bellows. The bellows was structurally reinforced with three thin-walled Vespel SP1 tubes connecting the evaporator to the ⁴He cold-plate.

Due to size constraints within the cryostat, the sealed ³He refrigerator was coupled to an external tank to prevent overpressurization. The pressure of the combined vessels at room temperature was 745 KpA; a factor of 4 times smaller than the elastic limit of the bellows. The condenser was directly coupled to the ⁴He coldplate. The sorption pump consisted of 131 gm of activated charcoal. The grains of charcoal were glued with Stycast to closely spaced copper fins which maximize the pump area. Calculations show that optimal sorption is achieved with at least 3 grams of charcoal per STP liter of gas (Duband (1990), private communication).

The pump was thermally linked to the ⁴He coldplate with a ultra-high purity tin wire. The thermal conductivity of tin decreases rapidly with temperature. The tin wire was a poor thermal link for temperatures above 10 K. The refrigerator was cycled by first heating the charcoal to 40 K for ~30 minutes, which desorbed the ³He from the pump. After heating, the charcoal and tin slowly cooled back to the ⁴He coldplate temperature. Meanwhile, the desorbed atoms condensed into liquid and pooled into the evaporator. Once the charcoal had cooled below 10 K, it pumped on the ³He, which cooled the liquid to ~300 mK. The refrigerator maintained this base temperature for 1.5-2 days with an unpumped ⁴He bath, and had a cooling capacity of 25 J.

5.1.2. ADR

We used of an adiabatic demagnetization refrigerator (ADR) developed in Berkeley as a prototype for the Space Infrared Telescope Facility (SIRTF). This ADR was flown multiple times on the MAX experiment. The details of the construction and testing of the MAX/MAXIMA ADR are found in Timbie, Bernstein, & Richards (1990) and Hagmann & Richards (1995).

The ADR consisted of a paramagnetic salt pill inside a superconducting magnet. The salt pill was made from 40 gm of ferric ammonium alum (FAA), and was supported within the shielded coil with a kevlar string suspension that was thermally intercepted by the ³He refrigerator cold-stage. The ⁴He cooled superconducting Nb-Ti coil generated a peak field of 2.5 T with a current of 6.2 A. The ADR was thermally cycled with a remotely commandable current controller. During cycling, the heat of magnetization was dumped to the ³He refrigerator cold-stage. The ADR had a laboratory tested hold-time of 17 hours and a flight-tested hold-time of 12 hours at ~100 mK with a ~ 90% duty cycle. The ADR had a cooling capacity of 0.093 J.

The wiring from the outside of the cryostat to the magnet was designed to minimize thermal conductivity and electrical power dissipation. The magnet current entered the cryostat through hermetic connectors and was carried by bundles of standard 22 AWG copper wire heat-sunk to the liquid N₂ coldplate. Each bundle of wire was soldered to a high-Tc superconducting lead (YBCO) (Eurus Monoco (U.S.A.)) clamped between the liquid N₂ coldplate and the top of the liquid ⁴He tank. The magnet current was then carried by formvar coated copper clad Nb-Ti superconducting wire which was heat-sunk to the side of the liquid ⁴He tank. The Nb-Ti leads were potted in Eccosorb CR-124 before entering the ⁴He cold-plate area, in order to filter RFI.

All of the wiring from the high-Tc leads to the magnet coil was superconducting during cryogenic operation. Any significant electrical power dissipation was dumped into the liquid N₂.

5.2. Bolometer wiring

The signals for each bolometer entered the cryostat via hermetic connectors. Once inside the cryostat, the signals were carried by a harness of low thermal conducting stainless steel wire (Cooner Wire (U.S.A.)) heat-sunk at its midpoint to the liquid N₂ thermal stage. The signals were then carried in Kapton wire striplines of 50 μ gold plated Ni wire, fabricated by Tayco Co. (U.S.A.), which

were potted in Eccosorb CR-124 (Emerson & Cuming Microwave Products (U.S.A.)). These modules were heat-sunk to the ^4He cold-plate and blocked radio frequency interference signals (§5.5).

The wiring between the RFI filters and the JFET modules (§5.6) was standard Teflon-coated multi-strand copper. The signals were then carried from the JFET module to the ~ 100 mK array via formvar coated 50 μ platinum tungsten wire (California Fine Wire (U.S.A.)), which had a low thermal conductance. The wiring between the JFETS and the bolometers was susceptible to microphonics. We bundled and twisted the wires for the bolometers around four thin walled G-10 tubes that were rigidly connected to both the JFET module and the array. The tubes were thermally intercepted by an OFHC copper heat strap from the 0.3 K thermal stage.

The wiring continued from the G-10 tubes to each photometer on four G-10 printed circuit boards with 0.25 mm copper traces. We covered both sides of the circuit board with electrically insulated aluminum tape to reduce the emissivity of the array. More details on wiring inside the MAXIMA cryostat can be found in Winant (2003).

5.3. Housekeeping thermometry

We monitored the internal temperatures with various cryogenic thermometers; we used silicon diodes at 77 K, carbon composition thermistors at 2 K to 4 K, an RuO₂ thermometer for the ^3He refrigerator (0.3 K), and a germanium thermistor for the ADR (0.1 K). Thermometer leads entered the cryostat through the same hermetic connectors as the bolometer signals. They were then carried by the same stainless steel wire harness and Eccosorb RFI filter module into the cold-plate area. Each device was wired to the RFI module with low thermal conducting Teflon coated 0.125 mm manganin wire (California Fine Wire (U.S.A.)). The wires for the 0.1 K thermometer were heat-sunk midway on the ^3He refrigerator cold-stage.

5.4. Internal Relative Calibrator

Bolometer responsivity varied over the duration of a flight, primarily because of variations in the temperature of the ~ 100 -mK ADR. These variations were monitored using a stable internal calibration source (*i.e.* a stimulator) consisting of a thin nickel-chromium layer (2 mm \times 2 mm) backed with a sapphire substrate. The metal layer was impedance matched to radiate efficiently into free space when heated. When a heating current ~ 1 mA was applied, the metal warmed to ~ 50 K with a time constant of ~ 1 sec. The heating current was maintained for 10 seconds, and was applied every 20 minutes during flight. The stimulator was mounted inside the cold optics box, and was fitted with a light pipe to illuminate the focal plane array from just outside the optical path. The illumination of the array was not uniform, with detectors closer to the calibrator receiving about twice the flux of the more distant detectors.

The source was extremely stable with negligible resistance fluctuations and $<1\%$ current fluctuations. The on-state calibrator temperature was further stabilized by a weak, temperature dependent thermal link to the liquid helium stage.

The absolute flux was not well measured, so the stimulator was used purely for monitoring of responsivity variations over time. Absolute calibration was obtained from celestial sources (the CMB dipole and planets). The use of stimulator data in detector calibration is discussed in §6.3.

5.5. RFI protection

During flight, several radio transmitters were used for telemetry. Each radiated 15 to 40 Watts at frequencies of 1.5 GHz and higher. Extensive filtering was required to prevent pickup from these sources in the detectors.

The receiver itself consisted of three metallic shells which served as partial Faraday cages. External cabling was also fully enclosed in a metallic shell. All cables between the receiver and the readout electronics and all cables exiting the readout electronics passed through commercial RF filtered connectors (Amphenol FPT02 Series; 60-dB attenuation at 1.0 GHz). Within the receiver, all wiring was potted in 27 cm of Eccosorb CR-124, a metal-filled epoxy commercially available from Emerson and Cuming, that acts as a radio frequency low-pass filter (30-dB attenuation at 1.0 GHz).

The optical window acted as a high-pass filter for ambient RFI, which had a measured cut-off of ~ 2.5 GHz. Higher frequency RFI in the optical path was blocked by taping a cylindrical sleeve made from multiple layers of 25 μ sheets of aluminized mylar around the perimeter of the optical path near the cryostat window with aluminum tape (Figure 16). This attenuated the coaxial transmission of RF between the shields without significantly compromising the thermal isolation between the different temperature stages inside the cryostat.

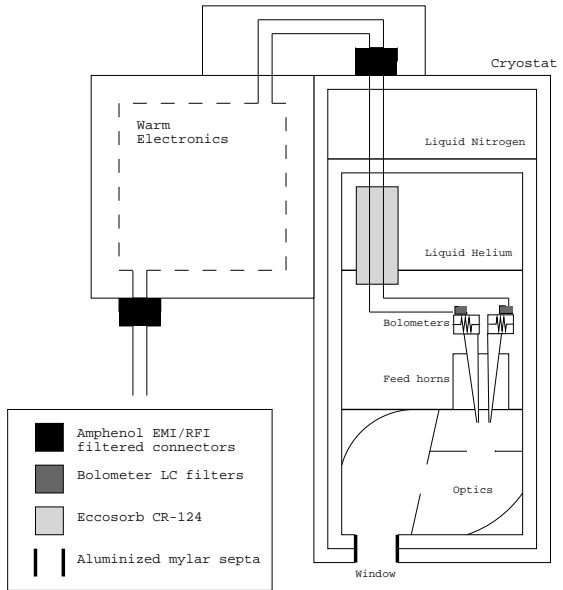


FIG. 16.— The bolometers (shown with resistor symbols) were shielded from electrical RFI pickup by three different types of filters in series, shown as filled rectangles. RFI was prevented from coaxially transmitting between the temperature baffles by contiguous layers of aluminized mylar placed around the optical path at the cryostat window. The cryostat and the warm electronics shield acted as Faraday cages.

Each individual bolometer was enclosed in a RFI-tight cavity. The optical opening into the cavity was small

enough to prevent RFI at frequencies below 100 GHz from radiatively coupling onto the bolometers. The bolometer signals were filtered at the cavity wall by LC feed-through filters. Calculations of the high frequency performance of these filters including distributed reactances were made by Hristov (1999), private communication.

These measures were only partially implemented before MAXIMA-I. The aluminized mylar septa and bolometer cavity LC filters were incorporated after MAXIMA-I and before MAXIMA-II. Tests revealed that detectors with LC filters showed dramatic improvement. The LC filters appeared to suppress pickup at $1 < f < 2$ GHz in both optical and dark detectors. We determined that the septa and LC circuits contributed at least 20-dB suppression of pickup in this frequency regime. The LC circuits were shown not to introduce measurable suppression or phase shifts in the signal band of the detectors.

This evidence supports the model that during MAXIMA-I, RFI leaked in through the window, around the temperature baffles, and then coupled into the bolometer wiring. This is believed to have caused the small, scan-synchronous signal seen by some MAXIMA-I detectors (§4.2).

5.6. Bias and Readout Electronics

The analog bolometer readout electronics were designed by V. Hristov from CalTech. The bolometers were AC-biased to minimize low frequency noise contributions from the electronics (e.g. $1/f$ noise in the JFET amplifiers). AC bias does not cause fluctuations in the bolometer temperature, assuming constant optical power and $f_{bias} \gg 1/2\pi\tau_{bolo}$. All detectors were biased at the same frequency by a single sine wave oscillator which could be tuned from 250 Hz to 400 Hz. We set this frequency before each flight to minimize microphonic noise.

The bias voltage amplitude for each detector was set between 50 mV and 100 mV by a potentiometer. Bias current variations were adequately controlled by two $40 M\Omega$ load resistors in series with each bolometer. The largest fractional change in bias current, observed during the MAXIMA-I planet scan, was of order 10^{-5} .

We minimized the microphonic sensitivity of the receiver by reducing the output impedance of the bolometers. This was achieved with a matched pair of cooled monolithic-dual silicon EJ-TIA JFET amplifiers (Infrared Laboratories (U.S.A.)) in a matched emitter follower circuit. The JFET pairs were packaged in standard transistor cans with internal thermal isolation and were cooled by a weak thermal link to the liquid ^4He bath, for an operating temperature of 150 K. Each JFET pair consumed $300 \mu\text{W}$ of power and contributed $6-10 nV Hz^{-0.5}$ to the total noise per channel.

The bolometer signals were further processed by ambient readout electronics. They were pre-amplified with an AD624 op amp, band-pass filtered around the bias frequency, and then were each rectified with an AD630 lock-in amplifier referenced to the bias signal.

Bolometer resistance fluctuations appeared in the side bands of the bias frequency, as determined by the telescope scan speed. Given the primary mirror modulation frequency of 0.45 Hz and peak velocity of 4 deg sec^{-1} (or ~ 25 beam FWHM per second), the data were in the range of 0.1-20 Hz around the bias frequency. Sig-

nals outside the band were suppressed by a four pole Butterworth filter with a characteristic frequency of 19.96 ± 0.61 Hz, averaged over all 20 read-out channels.

Finally, the rectified signal was amplified by a gain of 1800 and split to two outputs. We removed the offset from one signal stream with a single pole high-pass filter with a characteristic frequency of 14.9 ± 0.7 mHz, averaged over all 20 read-out channels. This signal was further amplified by a factor of 36, yielding a net gain of 65,000. Overall, the gain of the readout circuit had a temperature stability of $< 10^{-5} (\text{ }^\circ\text{C})^{-1}$.

5.7. Supporting Electronics and Telemetry

Bolometer signals were amplified, rectified, and digitally sampled with 16-bit resolution every 4.8 ms. Other data, including cryostat housekeeping, ambient temperatures, bolometer bias monitors, primary mirror position, electronics status, and low gain bolometer signals were sampled every 19.2 ms. The data were multiplexed and transmitted to a ground based data recording station over a 1.8-GHz radio downlink at a data rate of $160 \text{ kbits sec}^{-1}$. A separate 1.5-GHz downlink transmitted for the data from the pointing system and from balloon facility support systems. Video signals from pointing sensors were transmitted at 2-3 GHz, but were not transmitted during CMB scans to minimize the ambient radio frequency radiation. Control of the telescope from the ground was maintained via intermittent command signal at ~ 500 MHz.

The digitization and multiplexing data acquisition system was built at the Lawrence Berkeley National Laboratory, while telemetry and commanding systems were provided by the National Scientific Balloon Facility.

6. CALIBRATION

Absolute responsivity calibration used two known sources during each MAXIMA flight: the CMB dipole and a planet. Measurements of the CMB dipole gave the best absolute calibration for the 150-GHz and 240-GHz detectors. Observations of planets (Jupiter in MAXIMA-I and Mars in MAXIMA-II) were used to calibrate the 410-GHz detectors, and were used as a consistency check for the dipole calibration. The internal millimeter wave source (the stimulator described in §5.4) was used to periodically measure responsivity changes.

The MAXIMA-I data have a calibration error of 4%, while the MAXIMA-II data have a calibration error of 3%. These are the most accurate calibrations achieved by any sub-orbital CMB experiment. The MAXIMA calibrations are consistent with that of WMAP (Abroe et al. 2003).

6.0.1. Linearity

All calibration sources used for MAXIMA are significantly brighter than CMB fluctuations. Planet calibrations and stimulator events added enough loading to measurably reduce detector responsivity. These linearity changes are summarized in Table 11, and their impact on the calibrations is discussed in §6.1.2 (dipole), §6.2.1 (planets), and §6.3.1 (stimulator).

6.1. CMB Dipole

The dipole was the main calibrator for the 150-GHz and 240-GHz detectors, using the amplitude measurement of the COBE satellite (Smoot et al. 1991). Dipole

TABLE 11
CALIBRATION LINEARITY

Planet	Stimulator
Responsivity	Responsivity
Change	Change
(MAXIMA-I/MAXIMA-II)	(MAXIMA-I/MAXIMA-II)
150 GHz	0.7-2.5%/0.2-0.5%
240 GHz	1.0-6.1%/0.2-0.4%
410 GHz	1.9-7.7%/0.4-1.0%

Note.- Quoted values were derived from the maximum of the signal for MAXIMA-I (before the slash) and MAXIMA-II (after the slash). Ranges represent variations between detectors. For the dipole calibration the upper limit on nonlinearity was $\sim 0.05\%$.

observations were carried out by rotating the telescope in azimuth with an azimuthal angular velocity of $20^\circ \text{ sec}^{-1}$. The observed signal from the dipole was a sine wave at 56 mHz. We observed the dipole at an elevation of 50° in MAXIMA-I (to avoid side-lobe response from the Moon at lower elevation) and at 32° in MAXIMA-II. During MAXIMA-I the dipole, including the motion of the Earth around the Sun, had a magnitude of 3.195 mK and was tilted 20° from the horizon; the observed amplitude over the scan region was 2.04 mK. During MAXIMA-II the dipole had a magnitude of 3.010 mK and was tilted 48° from the horizon; the observed amplitude was 1.15 mK.

The rotating scan pattern of the dipole observation was sensitive to parasitic signals from Galactic dust and in some cases the atmosphere. The Galactic dust signal was modeled from frequency extrapolations of published maps (Jaffe (1999), Schlegel, Finkbeiner, & Davis (1998)). The dust signal was much smaller than the dipole signal at 150 GHz, except near the Galactic plane. Data within 5° of the Galactic plane were neglected in data analysis. Elsewhere, the dust model was fit to the data along with the dipole model. Overall normalization was taken as a free parameter to account for uncertainties in the frequency extrapolation of the dust signal. In practice, the dust model did not affect the dipole calibration due to its low amplitude and lack of a dipole-like spatial component.

An additional small signal was observed in the beginning of the MAXIMA-I dipole calibration. In MAXIMA-I we began the dipole observation near the beginning of the flight, while the telescope was still ascending from ~ 21.5 km to the final observing altitude of ~ 38.5 km. The additional signal was observed during the first third of the observation (altitude < 30 km). We believe that this signal was atmospheric for four reasons: (1) it was highly correlated in all the optical bolometers; (2) it was spectrally consistent with atmospheric emission, being larger for the higher frequency detectors; (3) it was spatially stable on the scale of a few minutes, but varies on longer scales; (4) the magnitude of the signal declined steadily with altitude.

The atmospheric signal was corrected using data from the 410-GHz bolometers. These data, which were relatively insensitive to the dipole and sensitive to the atmospheric signal, were used as a template for the signal in the 150-GHz and 240-GHz data. A correction was ap-

plied for the CMB sensitivity of the 410-GHz detectors, as calibrated by planet observations. As with Galactic dust, we found that fitting the atmospheric signal did not affect our final dipole calibration values. It did, however, increase calibration uncertainty, because of noise in the 410-GHz data used to model the effect.

6.1.1. Dipole Data Analysis

During each flight, the dipole was observed for ~ 30 minutes (100 rotations). For each detector, the effects of electronic filters and bolometer time constants were first deconvolved from the entire data stream. Data from each rotation were then fit independently according to the model,

$$T_{\text{detector}} = (A * T_{CMB,\text{Model}}) + (B * T_{dust}) + (C * N_{\text{drift}}) + D, \quad (2)$$

in which T_{detector} is time stream of detector data in voltage units, $T_{CMB,\text{Model}}$ is the CMB dipole model in units of temperature contrast, T_{dust} is the Galactic dust model, N_{drift} is linear drift, and A, B, C, D are fitting constants. A is the calibration of the detector to CMB signals.

For MAXIMA-I the atmospheric signal was taken into account by modifying the fit to,

$$T_{\text{detector}} = (A * T_{CMB,\text{Model}}) + (B * T_{dust}) + (C * N_{\text{drift}}) + D + (E * T_{410}). \quad (3)$$

T_{410} is time stream data from a 410-GHz detector and E is an additional fitting parameter. Because the 410-GHz data do have some very small sensitivity to the CMB, A is no longer an unbiased calibration. To account for this, the 410-GHz data are first calibrated using planet data and the parameter A is corrected,

$$A' = A - (E * \text{Cal}_{410}). \quad (4)$$

Cal_{410} is the planet-based calibration of the 410-GHz data and A' is the true calibration of the low frequency channel. In practice the 410-GHz term does not affect calibration values by more than 0.5σ , though it does increase uncertainties. The correction from A to A' has a negligible effect on both the calibration and the calibration uncertainty due to the small value of the E parameter.

Each rotation yielded a calibration value (A or A' above) and an associated error range. These were combined statistically, with $2-\sigma$ outliers excluded. Data from ~ 80 rotations were analyzed from each flight, with 2 to 8 excluded as outliers for each detector.

Data from the MAXIMA-II dipole observation are shown in Figure 17.

6.1.2. Dipole Calibration Error Sources

Dipole calibration uncertainty (1-4% depending on the detector) was dominated by detector noise at the dipole observation frequency of 56 mHz. The fitting routine was found numerically to reject noise beyond a fractional bandwidth of ~ 0.5 . Noise was effectively reduced by a further factor of $\sqrt{2}$ by the known phase of the dipole model. Raw detector noise near 56 mHz for a 150-GHz bolometer was typically $150 \text{ nV Hz}^{-0.5}$. Considering bandwidth and phase constraints, this yielded an

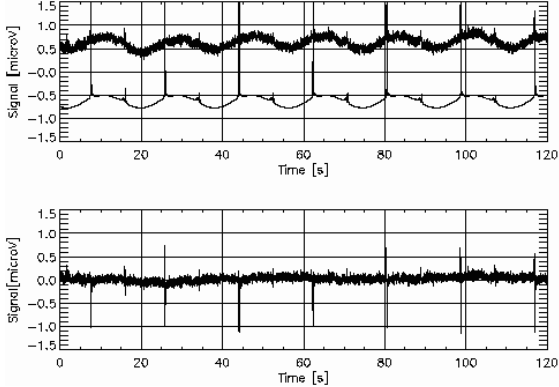


FIG. 17.— MAXIMA-II 150-GHz dipole data and fit. **Top panel:** The top trace is the data from a 150-GHz bolometer during observations of the CMB dipole. An overall gradient is removed and the offset is arbitrary. The sinusoidal signal is the CMB dipole modulated by the rotation of the telescope (~ 18 second period). The large spikes are caused by dust near the Galactic plane. The lower trace is a fitted model curve, including the CMB dipole and a Galactic dust map. **Bottom panel:** The difference between the model and the fit in the top panel are shown. The model deviates from the data near the Galactic plane crossing which are not well fit with the $\sim 10'$ pointing reconstruction accuracy of the dipole observation.

expected ~ 20 -nV noise level for a single dipole fit. For a typical 150-GHz detector the amplitude of the dipole response was ~ 70 nV. We therefore expected a statistical uncertainty of $\sim 30\%$ from a single rotation.

Detector noise was the only source of statistical uncertainty in the calibration, and could be estimated directly from the scatter of the individual, single rotation calibrations. Such analysis yielded single rotation statistical uncertainties of 10% to 30% for 150-GHz detectors in either flight. These numbers were somewhat lower than predicted due to imperfect understanding of detector noise at very low frequencies.

An integration of 80 to 90 dipole observations per flight provided a total statistical uncertainty of 1.4% to 4.2% for 150-GHz detectors in MAXIMA-I and 1.1% to 2.5% in MAXIMA-II. Because the CMB responsivity of the 240-GHz detectors was 60-70% that of the 150-GHz detectors, they had a proportionally higher statistical error. When combining data from multiple detectors, we used the highest statistical uncertainty of the combined channels. For MAXIMA-I, the modelling of the atmospheric signal increased the final calibration uncertainty by only about 0.5%.

In addition to statistical uncertainty, there were a number of known systematic effects, though none had a significant impact on the calibration. First, dipole pointing reconstruction was accurate to $\sim 10'$ and contributed negligibly ($\sim 0.1\%$) to the calibration uncertainty. Second, the signal from the dipole was small enough that bolometer saturation was negligible. Third, the dipole model derived from the COBE measurement was accurate to 0.68%. Finally, a ~ 15 mHz single-pole high-pass filter in the bolometer readout electronics was characterized to $\sim 0.3\%$ at the dipole scan frequency. Though this was tested under laboratory conditions, where the electronics were substantially cooler than in flight, the temperature coefficients of the filter caused at most a 1% shift in filter pole frequency in flight. This maximum

shift would have caused only a 0.08% change in response magnitude and 0.16° change in phase.

6.2. Planets

In each flight observations were made of a planet: Jupiter in MAXIMA-I and Mars in MAXIMA-II. The planet observation procedure has been described in §3.3.1. Responsivity calibration was obtained from the maximum voltage response. Expected signals were derived from published measurements and models of planet temperatures and emissivities (Goldin et al. (1997), Wright & Odenwald (1980), Rudy (1987)), combined with the spectral response of the detectors. A correction was applied for beam dilution, i.e. the fraction of the telescope beam filled by the planet. Jupiter had an angular diameter of $46.5''$ during MAXIMA-I and Mars had an angular diameter of $12.7''$ during MAXIMA-II. The dilution factors varied from 3.4×10^{-3} to 4.4×10^{-3} for MAXIMA-I and 3.1×10^{-4} to 4.1×10^{-4} for MAXIMA-II. This correction is the dominant error source for the planet calibration in both flights.

An additional correction of roughly 5% for MAXIMA-I and 1% for MAXIMA-II was applied for the reduction in responsivity caused by the optical load from the planet (Table 11). This effect was neglected in the initial MAXIMA-I data analysis and caused an apparent small systematic discrepancy between the dipole and Jupiter calibrations. This discrepancy was within the error range of the Jupiter calibration and did not affect the CMB map or power spectrum.

6.2.1. Planet Calibration Error Sources

The dominant error term for the planet calibration is the uncertainty in the beam dilution factor. The uncertainty in the integrated beam response is 5% to 10%. In addition, there is a possibility of small, broad side-lobes that are not measured in the beam maps. We assign an uncertainty of 10% from beam shape errors. Beam shape error, especially that due to broad side-lobes, is partially correlated between detectors because of their shared optics.

Uncertainties in the effective brightness temperature of the planets contribute 5% to calibration error. The brightness temperature of Mars has been modeled to this accuracy, both by extrapolation from high frequency observations (Wright & Odenwald 1980) and by physical modeling Rudy (1987). The atmospheric properties for Jupiter make modeling relatively difficult. Our expected Jupiter signal is based on published brightness ratios between Jupiter and Mars (Goldin et al. 1997). The planet temperature uncertainty is fully correlated between all the detectors.

Measurements of the detector spectra contribute 1-2% error at 150 GHz, 3-7% at 240 GHz, and 2-3% at 410 GHz. Measurements of the peak planet voltage contribute 1-4% error; one detector in MAXIMA-II is anomalously noisy, increasing this term to $\sim 10\%$. Uncertainty in the bolometer saturation is negligible.

6.3. Time Dependent Calibration

The responsivity of bolometers varied by 1-2% for a change of 1 mK in the thermal reservoir temperature. The temperature varied by ~ 6 mK over the course of

data collection in MAXIMA-I and by ~ 21 mK in MAXIMA-II.

Responsivity variations were monitored using the internal millimeter wave source (stimulator) described in Section 5.4.

To obtain relative calibration values from stimulator events, we began by subtracting an overall gradient from each event to remove the effects of detector drift. We then performed a linear fit between pairs of stimulator events. The slope of this fit was the calibration ratio between the events, while the offset of the fit was simply an offset in the detector data.

Once the relative calibration at each stimulator event was known, we fit the values to a linear function of the temperature of the bolometer thermal reservoir (Figure 18). This fit was combined with the absolute calibration to obtain the overall calibration as a function of time throughout the flight (§6.4).

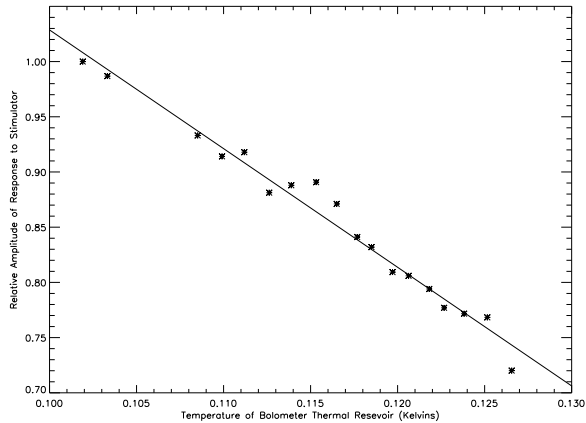


FIG. 18.— Temperature dependence of the responsivity of a 150-GHz detector. These data were collected during MAXIMA-II. The point near 0.127 K, measured shortly after sunrise, showed less responsivity than would be expected from the nighttime data. During MAXIMA-I, the temperature of the thermal reservoir was more stable, varying from 98–104 mK.

6.3.1. Relative Calibration Error Analysis

The relative calibration between stimulator events was affected by random variations (detector noise or stimulator instability), but was not affected by systematics that are consistent between stimulator events, such as uncertainties in the spectra of the detectors and the beam filling of the stimulator signal. The reduction in bolometer responsivity due to the large optical load of the stimulator was nearly stable (Table 11). Though it did vary with bolometer temperature, this variation contributed less than 0.1% error to the relative calibration.

Random errors in the comparison of stimulator events were 1–2%. Instabilities in the stimulator current accounted for $<0.5\%$ of this, while detector noise accounts for the rest.

We treated the relative calibration as a linear function of temperature and took the optical load during the flight as constant. These assumptions were supported by bolometer models (Winant (2003), Grannan (1997)) and contributed negligibly to calibration error.

6.4. Combined Calibration

The overall calibration for each detector was obtained by combining an absolute calibrator with the relative calibration. The absolute calibrator was the CMB dipole for 150-GHz and 240-GHz detectors and was the planet scan for 410-GHz detectors. The relative calibration was based on the temperature of the bolometer thermal reservoir and the responsivity-temperature relation obtained in Section 6.3. Temperature was monitored continuously.

The overall calibration error was the combined error from the absolute calibrator and the relative calibration. Relative calibration error varied over the course of the flight. Quoted values are based on averages over the CMB observations. Relative calibration error was sub-dominant for MAXIMA-II (1% to 2%) and was negligible for MAXIMA-I ($<0.1\%$).

The published MAXIMA-I data were conservatively assigned the highest calibration uncertainty of the detectors used, 4%.

7. SCANS AND POINTING

7.1. Scan Strategy

Each CMB observation was conducted at a fixed elevation, while the telescope beams were moved in azimuth. The azimuth modulation defined one dimension of the roughly rectangular scan region. The rotation of the sky over the duration of the observation defined the other dimension.

The azimuth motion consisted of two independent modulations. The primary mirror rotation provided a relatively fast modulation with a frequency of 0.45 Hz and a peak-peak span of 4.0° . The motion of the entire telescope provided slower modulation at frequencies from 12 mHz to 25 mHz, depending on the scan parameters, with peak-peak spans of 4.5° to 9.0° . The fast modulation prevented our data from being significantly corrupted by low frequency noise. Taken together, the two made our data relatively robust against modulation synchronous parasitic signals.

The two CMB scans of each flight observed the same region of the sky, but at different times and at different elevation angles. The rotation of the sky between these observations caused the two scans to be tilted relative to each other in sky-stationary coordinates. The average angle of cross-linking was 22° for MAXIMA-I and 27° for MAXIMA-II.

The two azimuth modulations, the rotation of the sky, and the cross-linked revisit were uncorrelated and are on radically different time scales, minimizing the effects of potential scan-correlated systematics.

Depth of integration was set by the total width of the combined azimuth modulation and the rotation rate of the sky. The average integration time per beam-size was ~ 2.5 seconds in MAXIMA-I and ~ 2.2 seconds in MAXIMA-II. This led to an average expected noise level of $\sim 60 \mu\text{K}$ per beam size area for our best single detector and $\sim 40 \mu\text{K}$ for our published combination of four MAXIMA-I detectors. In practice, integration was several times longer in the center of the observed region and shorter near the edges.

7.2. The Attitude Control System

The pointing system, or attitude control system (ACS), served both to control the orientation of the tele-

TABLE 12
POINTING PERFORMANCE

CMB Observation	MAXIMA-I Scan 1	MAXIMA-I Scan 2	MAXIMA-II Scan 1	MAXIMA-II Scan 2
Max Scan Speed (deg sec ⁻¹)	0.29	0.30	0.29	0.26
RMS Velocity Error (")	0.022	0.028	0.043	0.057

scope in flight and to acquire the data needed for post-flight pointing reconstruction. The pointing system consisted of attitude sensors, a central feedback loop control computer, and motors. Some of the easily interpreted sensors were used in pointing control, while the most precise sensors, the CCD cameras, were used after the flight for pointing reconstruction. The ACS was originally constructed at IROE-CNR (now IFAC-CNR) and Università di Roma La Sapienza, in Italy. The system was similar to that used in the BOOMERanG experiment (Crill et al. 2002).

A computer read data from the various sensors, applied a digital feedback algorithm, and set the power level for the motors. Each of these tasks was performed once every 96 ms, synchronously with the bolometer data acquisition system.

Signals from most sensors were sampled each cycle. Data from the CCD cameras were processed by a separate computer, and were passed to the control computer every two cycles (192 ms). GPS data (absolute time and position) were updated once per second.

Pointing normally followed one of several preprogrammed flight schedules. Remote (ground-based) commanding was used to switch between, modify, or override schedules. In addition, remote commanding was used to modify control loop gains, to make adjustments to sensor calibrations, and to set parameters for the CCD image processing.

Feedback control was based on azimuthal rotation velocity, as measured by a rate gyroscope. The gyroscope had an accuracy of $\sim 0.01^\circ$ sec⁻¹. Though they were very sensitive, the gyroscopes had substantial low frequency drifts, primarily due to ambient temperature fluctuations. Drifts were calibrated once per gondola scan period, and had little impact on pointing control. Two other gyroscopes, measuring pitch and roll velocities, were not used in feedback control. The performance of the feedback control loop is summarized in Table 12.

Absolute azimuth was measured in real time using a two axis magnetometer. The magnetometer was extremely precise ($< 0.5'$) in differential measurement, but was highly non-linear due to the magnetic properties of the telescope. Pre-flight measurements were used to calibrate the magnetometer to an accuracy of $\sim 30'$.

Absolute elevation was measured in real time by an optical angle encoder between the inner assembly (receiver and primary mirror) and the outer frame of the telescope. The accuracy of this measurement depended on the balancing of the telescope ($\sim 0.1^\circ$) and on long time scale pendulum motion ($\sim 0.5^\circ$, varying over tens of minutes). The differential accuracy of this elevation measurement was $\sim 1'$.

7.2.1. CCD Cameras

The CCD star cameras provided the most accurate measurement of telescope orientation and were used for post-flight reconstruction. One camera was mounted on the inner telescope assembly and was boresighted with the telescope beams when the primary mirror was in its central position. The second camera was positioned on the outer frame so that north celestial pole star (Polaris) was in the camera's field of view during CMB observations - approximately 40° to the right of the boresight, at a fixed elevation angle of about 31° .

The boresighted camera data were used for the final pointing reconstruction and were accurate to $\sim 0.5'$. The secondary camera was only accurate to $\sim 15'$, due to the offset of the measurement from the telescope boresight combined with pendulum motion of the telescope. Secondary camera data were used to identify stars in the primary camera.

The boresighted camera had a field of view of 7.17° by 5.50° with a pixel size of $0.84'$ by $0.69'$. The resolution was further improved to $\sim 0.5'$ in flight by software interpolation. The secondary camera had a larger field of view (14.34° by 11.00°) and lower resolution ($\sim 1.0'$).

The boresighted camera reliably detected stars of V magnitude 5.0 or brighter. Stars of V magnitude 5.0 to 6.0 were detected intermittently, and stars dimmer than V magnitude 6.0 were rarely detected. This sensitivity was sufficient to detect stars in all of the MAXIMA-I scan region and $\sim 80\%$ of the MAXIMA-II scan region. Source brightness was not an issue for the secondary camera, which always viewed Polaris (V magnitude = 2.0).

Image processing introduced a delay of ~ 200 ms to the camera data. The cameras internally sampled the CCD chips at 30 Hz, asynchronous to the rest of the system. This caused a jitter up to 33 msec in the image processing delay, for an overall delay of 200 ± 16 ms between pointing data and bolometer data. At our gondola scan speeds, 200 ms translated to $2'$ to $5'$ of gondola rotation, which is a significant fraction of our $10'$ beam-size and was taken into account. The ± 16 -ms jitter translated to $\sim 0.15'$ RMS pointing uncertainty.

7.2.2. Motors

Three motors were used to point the MAXIMA telescope and a fourth was used to modulate the primary mirror. They are shown schematically in Figure 19. Two motors, located near the top of the telescope frame, were used for pointing in azimuth. One of these drove a reaction wheel with a moment of inertia of 10 kg·m² ($\sim 0.5\%$ that of the telescope). The other torqued against suspension cables connected to the balloon, which had a much greater moment of inertia than the telescope. Both motors were direct drive (ungeared), had a peak torque of 33.9 N·m, and received a maximum power of ~ 50 W from the control system. The light reaction wheel provided fast response, while the other motor kept the speed of the reaction wheel low by transferring angular momentum into the balloon. The rotational velocities of these motors were monitored by tachometers.

Elevation control was provided by a geared motor connected to a linear actuator arm. The arm was fixed between the outer assembly of the telescope frame and the inner assembly of the receiver and primary mirror. The

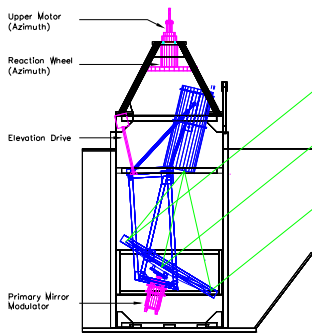


FIG. 19.— Two motors near the top of the telescope controlled azimuthal orientation by driving against a reaction wheel and the cables from the balloon, respectively. A linear actuator/servo-arm tilted the inner assembly, pointing the telescope in elevation. A motor below the primary mirror modulated it at relatively high speed (0.45 Hz, $\pm 2^\circ$ amplitude) in azimuth. The frames shown on the front and back of the telescope were far side-lobe baffles.

inner assembly was balanced about the rotation axis, so the static load on this motor was very small.

Motor power was determined in a digital control loop. Pointing control in azimuth and elevation were not strongly coupled and may be considered separately.

In azimuth, we used a rotational velocity-based proportional feedback system based on the rotational velocity measured by a rate gyroscope. In CMB scans, the target velocity was constant, except during turnarounds in the scan direction. During turnarounds the target velocity varied linearly with time. The absolute position was not used directly in the control loop; it was instead used to trigger these turnarounds. An additional feedback term proportional to the rotational velocity of the flywheel was applied to the upper motor, slowly transferring flywheel angular momentum to the balloon.

The elevation control formula was based on the measured angle of the telescope inner assembly relative to the outer frame. In this case, the power to the elevation drive was determined by a position-based proportion-derivative feedback loop.

The primary mirror was continuously rotated from side to side about the axis indicated in Figure 6 in Section 3. The motion was a rounded triangle scan with an amplitude of $\pm 2^\circ$ and a frequency of 0.45 Hz. This modulation superimposed on that of the entire telescope yielded the scan pattern in Figure 20. The resulting scan pattern in RA and Dec is shown in Figures 21 and 22.

Because the mirror rotation axis was not vertical, there was also a small modulation in elevation - a bowed pattern in which the extremes of the mirror modulation rose slightly in elevation. The elevation motion could in principle have led to a scan synchronous signal in the bolometers due to atmospheric emission. In practice, the elevation motion ($< 2'$) was not large enough to generate a detectable signal.

The mirror was actuated by a DC motor with solid state PID control electronics. The motor was obtained commercially and the control electronics were built at Berkeley. Mirror position was controlled to an accuracy of $1'$.

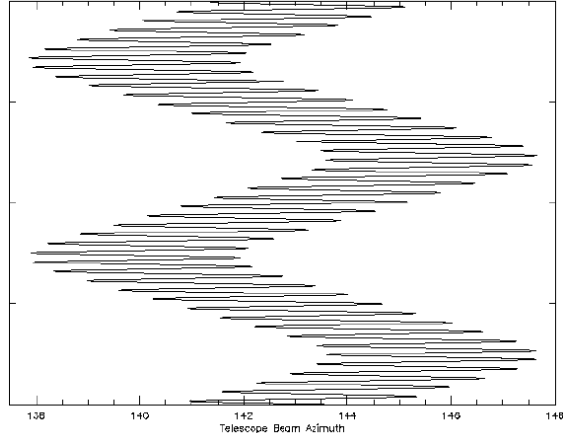


FIG. 20.— A simulation of the double modulation in azimuth. The x-axis is the azimuthal position of the telescope beams, while the y-axis is time. The slower modulation is caused by the motion of the entire telescope, while the faster modulation is caused by the rotation of the primary mirror about the optic axis.

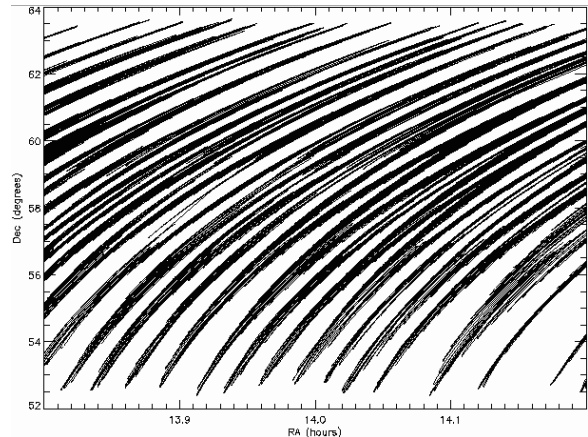


FIG. 21.— A MAXIMA-II scan pattern formed in RA and declination, combining the azimuth modulations with the rotation of the sky. Lines of constant elevation move with the rotation of the sky, spanning the plot in a diagonal arc from the lower left to the upper right. The gaps seen in this scan pattern are less than half the telescope beam size.

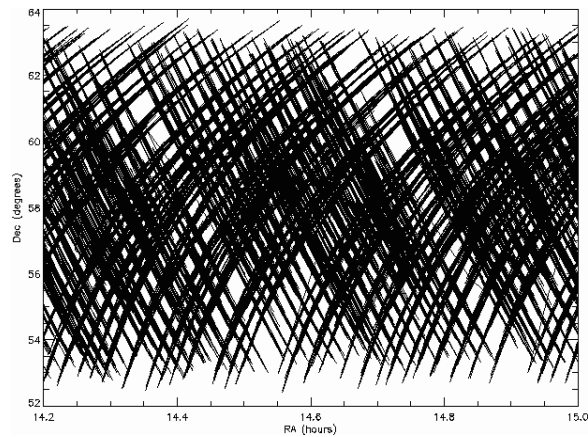


FIG. 22.— The cross-linked scan pattern from MAXIMA-II, consisting of two scans similar to that shown in Figure 21. The average cross-linking angle was 27° .

TABLE 13
POINTING RECONSTRUCTION UNCERTAINTIES

	Random Errors		Systematic Errors		
	CCD Camera ^a	Camera Timing ^b	Interpolation ^c	Detector Offset ^d	Primary Modulation ^e
MAXIMA-I	0.46'	0.15'	<0.001'	0.25'	0.81'
MAXIMA-II	0.58'	0.15'	<0.001' (~1')	0.25'	0.81'

^aCCD Camera-Error in image analysis.

^bCamera Timing- Uncertainty in time of image acquisition.
is the effect of the timing uncertainty of image acquisition.

^cInterpolation-<0.001' interpolation error applies to all of MAXIMA-I and ~80% of MAXIMA-II. The rest of MAXIMA-II had very few stars, increasing this term.

^dDetector offset-Boresight uncertainty.

^ePrimary Modulation-Uncertainty in mirror orientation.

7.3. Pointing Reconstruction

The complete pointing reconstruction for one detector for both MAXIMA flights can be seen in Figure 5.

Pointing reconstruction was based primarily on data from the CCD cameras. Often, pointing could be determined simultaneously from two different stars in the same field of view. In these cases the discrepancy between the two pointing solutions was used to estimate the overall error in the CCD measurement. The typical discrepancy was $\sim 0.5'$ (Table 13).

Between camera measurements, the telescope typically moved $\sim 8'$. In the azimuth, data from the rate gyroscope were integrated to find intervening positions. As a test of accuracy, the azimuth data were reinterpolated numerically and were compared to the gyroscope-based interpolation. The difference between the two was used to estimate the pointing error introduced by interpolation. Though the RMS discrepancy between these two methods was very small, the distribution had extreme outliers corresponding to regions of the sky with few bright stars. Interpolated regions with a difference of greater than $3.3'$ (one third of the FWHM beam size) were not used in data analysis.

In the elevation direction, the rate gyroscopes were more difficult to calibrate. However, the motion of the telescope in elevation was extremely slow and small, so these data were safely interpolated numerically.

Finally, the effect of the primary mirror modulation was included. The angle of the primary mirror was measured to several arcseconds by a linear variable differential transformer (LVDT). The LVDT data were calibrated both before and during flight using data from the planet observation.

The motion of the primary mirror moved the telescope beams primarily in azimuth. However, there was a small motion in elevation which was much more difficult to calibrate and was a source of pointing uncertainty. The elevation motion depended upon the zero position of the mirror. This was measured to $\sim 1^\circ$, which led to a conservative pointing uncertainty of about $0.8'$ RMS.

The $0.8'$ uncertainty of the primary mirror modulation was the largest source of error in the MAXIMA pointing solution. Though purely systematic, the scan pattern

and cross-linking tended to blur out the effect. In addition, other sources of pointing uncertainty further randomized the total error. The overall pointing error was approximated as a $1'$ Gaussian blur. End to end tests demonstrated that such a blur in leads to a 10% reduction in the CMB power spectrum at $\ell=1000$ and that this reduction scaled roughly as ℓ^2 , over the range where the fractional reduction is much less than 1.

Pointing uncertainty was a subdominant source of CMB power spectrum error at all values of ℓ . While it was possible to compensate the power spectrum for the reduction caused by pointing error, we have not done so because it was relatively small, and because our model of the pointing error as Gaussian is not exact.

8. SUMMARY AND DISCUSSION

The performance of MAXIMA-I provided a definitive measurement of CMB temperature anisotropy on sub-degree scales. High resolution maps, power spectra over multipoles of $35 \leq \ell \leq 1235$, and cosmological parameter estimates were generated from data from five of the sixteen photometers, as published in Hanany et al. (2000), Balbi et al. (2000), Lee et al. (2001), Stompor et al. (2001), and Abroe et al. (2002). Both intermediary and final results passed a series of systematic tests (Stompor et al. (2003), Abroe et al. (2003)), probing contamination from instrumental noise, from foregrounds or from the data analysis pipeline.

The 225 square degrees area of the sky that was scanned during the MAXIMA-2 flight in 1999 overlapped with 50 square degrees of the area scanned during MAXIMA-1 and was larger by about a factor of two, see Figure 5. The expected detector performance and scan strategy were similar between the two flights. However, the data showed a somewhat higher level of systematic effects, which would have required more effort to understand and overcome. The team has decided to release only limited results that will facilitate the comparison between the MAXIMA-1 and MAXIMA-2 maps (Abroe et al. 2003).

JHPW and AHJ acknowledge support from NASA LTSA Grant no. NAG5-6552 and NSF KDI Grant no. 9872979. PGF acknowledges support from the RS. BR and CDW acknowledge support from NASA GSRP Grants no. S00-GSRP-032 and S00-GSRP-031. MEA and RS acknowledge support from NASA grant no. NRA-00-01-AISR-004. MAXIMA is supported by NASA Grants NAG5-3941, NAG5-4454, by the NSF through the Center for Particle Astrophysics at UC Berkeley, NSF cooperative agreement AST-9120005. Computing resources were provided by the National Energy Research Scientific Computing center, which is supported by the Office of Science of the U.S. Department of Energy under contract no. DE-AC03-76SF00098, and by the University of Minnesota Supercomputing Institute in Minneapolis, Minnesota. MAXIMA field and flight support was provided by the National Scientific Balloon Facility. The MAXIMA team would like to thank P. Timbie for the use a Gunn oscillator. We thank P. Mauskopf for providing electronic readout units.

REFERENCES

- Abramowitz, M. & Stegun, I. A., Eds. 1972, Handbook of Mathematical Functions with Formulas, Graphs and Mathematical Tables, Dover Publications (New York)
- Abroe, M. E., et al. 2002, MNRAS, 334, 11
- Abroe, M. E., et al. 2003, ApJ, submitted (astro-ph/0308355)
- Balbi, A., et al. 2000, ApJ, 545, L1; Erratum-ibid. 558 (2001) L145
- Bock, J. J. 1994, Ph.D. Thesis, University of California, Berkeley
- Bock, J. J., Parikh, M. K., Fischer, M. L., & Lange, A. E. 1995, Applied Optics, 34, 4812
- Bock, J. J., Chen, D., Mauskopf, P. D., & Lange, A. E. 1995, Space Sci. Rev., 74, 229
- Cayon, L., Argueso, F., Martinez-Gonzalez, E., & Sanz, J. L. 2003, MNRAS, in press (astro-ph/0306164)
- Crill, B. P., et al. 2002, ApJ, submitted (astro-ph/0206254)
- Finkbeiner, D. P., Davis, M., & Schlegel, D. J. 1999, ApJ, 524, 867
- Galeazzi, M. & McCammon, D. 2003, J. Appl. Phys. 93, 4856
- Goldin, A. B., et al. 1997, ApJ, 488, L161
- Goldstein, J. H., et al. 2003, preprint (astro-ph/0212517)
- Grannan, S. M. 1997, Internat. J. IR. Millim. Waves, 18, 319
- Griffin, M. J., Bock, J. J. & Gear, W. K. 2002, Applied Optics, 41, 6543
- Hagmann, C., & Richards, P. L. 1995, Cryogenics, 35, 303
- Haller, E. E. 1985, Infrared Physics, 25, 257
- Halpern, M., Gush, H. P., Winshnow, E., & de Cosmo, V. 1986, Appl. Opt., 25, 565
- Hanany, S., Jaffe, A. H., Scannapieco, E. 1998, MNRAS, 299, 653
- Hanany, S., et al. 2000, ApJ, 545, L5
- Irwin, P. G. L. 1993, Infrared Physics, 34, 549
- Jaffe, A. H. 1999, "Microwave Foregrounds" (ASP, San Francisco)
- Jaffe, A. H., et al. 2001, Phys. Rev. Lett., 86, 3475
- Jaffe, A. H., et al. 2002, ApJ, submitted (astro-ph/0301077)
- Lee, C. 1997, Ph.D. Thesis, Queen Mary and Westfield College
- Lee, A. T., et al. 2001, ApJ, 561, L1
- Olver, A., Clarricoats, P. Kishk, A. & Shafai, L. 1994, Microwave Horns and Feeds (New York, New York: IEEE Press)
- Pardo, J. R., Cernicharo, J. & Serabyn, E. 2001, IEEE Trans. on Antennas and Propagation, 49/12, 1683
- Rabii, B. 2002, Ph.D. Thesis, University of California, Berkeley (astro-ph/0302159)
- Richards, P. L. 1967, in Spectroscopic Techniques for Far Infrared, Submillimetre and Millimetre Waves, ed. D. Martin (North Holland, Amsterdam), 33
- Richards, P. L. 1994, Journal of Applied Physics, 76, 1
- Rudy, D. J. 1987, Ph.D. Thesis, California Institute of Technology
- Rubino-Martin, J., et al. 2003, MNRAS, 341, 1084
- Santos, M. G., et al. 2002, Phys. Rev. Lett., 88, 241302
- Santos, M. G., et al. 2003, MNRAS, 341, 623
- Schlegel, D. J., Finkbeiner, D. P., & Davis, M. 1998, ApJ, 500, 525
- Sievers, J. L., et al. 2003, ApJ, 591, 599
- Smoot, G. F. et al. 1991, ApJ, 371, L1
- Spergel, D. N., et al. 2003, ApJS, 148, 175
- Stompor, R., et al. 2001, ApJ, 561, L7
- Stompor, R., et al. 2002, Phys. Rev. D, 65, 022003
- Stompor, R., Hanany, S., et al. 2003, C. R. Physique (Academie des Sciences, Elsevier), in press
- Timbie, P. T., Bernstein, G. M. & Richards, P. L. 1990, Cryogenics, 30, 271
- Welford, W. T. & Winston, R. 1978, The Optics of Nonimaging Concentrators: Light and Solar Energy (New York, New York: Academic Press)
- Wang, X., Tegmark, M., Jain, B., & Zaldarriaga, M. 2002, Phys. Rev. D, submitted (astro-ph/0212417)
- Winant, C. D. 2003, Ph.D. Thesis, University of California, Berkeley
- Wright, E. L., & Odenwald, S. 1980, BAAS, 12, 456
- Wu, J. H. P., et al. 2001a, Phys. Rev. Lett., 87, 251303
- Wu, J. H. P., et al. 2001b, ApJS, 132, 1